University of South Florida
Scholar Commons

Graduate Theses and Dissertations   Graduate School

4-7-2008

Micro-Autoradiographic Fusion Tomography

James Merker
University of South Florida

Follow this and additional works at: https://scholarcommons.usf.edu/etd

Part of the American Studies Commons

Scholar Commons Citation

www.manaraa.com

Micro-Autoradiographic Fusion Tomography

by

James Merker

A thesis submitted in partial fulfillment
of the requirements for the degree of
Master of Science in Mechanical Engineering
Department of Mechanical Engineering
College of Engineering
University of South Florida

Co-Major Professor: Frank Pyrtle, Ph.D.
Co-Major Professor: Jose Porteiro, Ph.D.
Daniel Hess, Ph.D.

Date of Approval:
April 7, 2008

Keywords: MCID Analysis, three dimensional (3-D) model, optical fusion,
VoxBlast, radiolabeled drug

Table of Contents

List of Figures

iii

iv

Micro-Autoradiographic Fusion Tomography

James Merker

ABSTRACT

Two-dimensional (2-D) micro-autoradiography is typically used to identify the location of a radio-labeled ligand bound to a cellular target in tissue sections. Data, such as a histological image, combined with the autoradiographic data provide a spatial relationship of the radiolabel to cellular structures. However, the disadvantage of 2-D imaging is that it only provides a local distribution of the radiolabel within a tissue slice, and not a volumetric regional distribution in the structure of interest. The development of 3-D autoradiographic/histological visualizations would provide important information not otherwise apparent, such as the ability to visualize the distribution of the labeled agents in subcutaneous tissue. We plan to obtain digital micro-autoradiographic images and fuse them to their corresponding histological images using commercially available software. We plan to create a series of 2-D fused images. This series of 2-D fused images will then form a basis for creating 3-D visualization of autoradiographic/histological images using another commercially available software. These type of fused 3-D images, which we will refer to as micro-autoradiographic fusion tomography (MAFT), are not currently available.

We will illustrate the use of MAFT with the distribution of vascular endothelial growth factor (VEGF) in subcutaneous tissue. [^{14}C]-VEGF will be injected into rat subcutaneous tissue. VEGF has been found to stimulate angiogenesis, or the growth of new blood vessels, which could prove beneficial by aiding the function of an implantable blood glucose sensor. The diffusion coefficient for VEGF in subcutaneous tissue has not yet been characterized. MAFT would be an ideal technique to use for this type of study.

My thesis will address the following specific aims: 1) To label the nicotine receptors in adult and adolescent rat brains, and to obtain digital micro-autoradiographic images and histological images; 2) To fuse a 2-D digital micro-autoradiographic image with a 2-D histological image; 3) To create a 3-D image from a series of 2-D fusion images; and 4) To assess the increased information value obtained using MAFT.

Chapter 1
Background and Significance

1.1 Medical Imaging

Medical imaging uses various techniques to directly or indirectly visualize the structure and function of tissue and organs. Structural imaging provides static information on the micro- and macroscopic anatomical structure of tissues and organs, and can be a valuable diagnostic tool for diseases (e.g. tumors) and injury. In contrast, functional imaging is used to discern alterations in living processes and can detect alterations in proteins and metabolic processes. In this Neurotechnology Research, Development, and Enhancement (R21) grant proposal, our focus is on functional imaging techniques of the brain.

Functional magnetic resonance imaging (fMRI) is a safe and totally noninvasive technique that images hemodynamic changes with MRIs. fMRI has recently become one of the most successful tools used to study blood flow and perfusion in the brain. Changes in neural activity are accompanied by focal changes in cerebral blood flow, blood volume, blood oxygenation, and metabolism. These changes can be used to produce functional maps of mental operation (Kwong and Chesler, 2002). At present, the resolution of fMRI is less than a millimeter (Aine, 1995). Future high-field fMRI scanners with field

1

strengths of 3T and beyond, and optimized acquisition techniques, will enhance the temporal and spatial resolution (Weiller et al., 2006).

In Positron Emission Tomography (PET) imaging, a biological molecule that carries with it a positron-emitting isotope (e.g. ^{11}C, ^{13}N, ^{15}O, or ^{18}F) is injected into the body (Budinger, 2000). Within a few minutes, isotope accumulates in an area of the body for which the molecule has an affinity. For example, glucose labeled with ^{11}C, or a glucose analogue labeled with ^{18}F, accumulates in regions where glucose is used as the primary source of energy such as in the brain or tumors (Young et al., 1999). PET measures the emissions and a computer uses the data to produce multicolored 2 or 3-D images of the distribution. PET scans are increasingly read alongside CT scans or MRI scans, the combination giving both anatomic and metabolic information (what the structure is, and what it is doing) (Connolly et al. 2000; Cunningham, 2000). PET has the significant advantage of being able to identify specific brain receptors by its ability to image radiolabeled receptor ligand binding to these proteins. Most commercially available PET systems have a resolution of approximately 4 mm (Aine, 1995). The greatest benefit of PET scanning is that different compounds can be used to image blood flow, and oxygen and glucose metabolism. These measurements reflect the brain activity in various regions of the brain. The biggest disadvantage of PET is that the radioactivity decays rapidly and hence, is limited to short monitoring tasks. Prior to fMRI, PET scanning was the preferred method of brain imaging.

2

Single photon emission computed tomography (SPECT) uses radiolabeled pharmaceuticals that distribute in different internal organs or tissues. SPECT uses gamma ray emitting radioisotopes and a gamma camera. The recorded data is used to construct 2-D or 3-D images by a computer. A major disadvantage of SPECT is its poor resolution (approximately 1 cm) (Tsui, 2000). SPECT can be register to CT images which can provide additional anatomical information (Cunningham, 2000). SPECT differs from PET in the types of radionuclides used. The disadvantage of PET is that it requires the use of tracers with a short half-life that must be produced in a cyclotron, and are expensive. Hence, both the performance and instrumentation of SPECT are less than PET.

1.2 Other Imaging Techniques

Like PET and SPECT, autoradiographic imaging and phosphor imaging can also identify the location of specific brain receptors by its ability to image radiolabeled receptor ligand binding to the receptor protein. The advantage of autoradiographic and phosphor imaging over PET and SPECT, is its high resolution. The disadvantage of autoradiographic imaging and phosphor imaging is that they are not techniques that can be used in the clinical arena.

For autoradiography, the location of beta-emitters and some soft gamma-emitters in biological tissue slices can be achieved by placing the section against x-ray film or by immersion in photographic emulsion. The exposure time is lengthy and a month is not uncommon for tritium labels. The film or exposed emulsion is then developed and the activity quantified by optical densitometry.

3

Film and emulsion response to radioactivity is nonlinear except over a narrow range following an S-curve. Activity standards must be run with each batch to achieve quantification. If the exposure time is too short or too long, falling towards the extremes of the S-curve, then quantification is not possible. With film, re-exposure is needed. With emulsions, the sample must be discarded and replaced. Time lost is a common occurrence.

The spatial resolution of film is quite good for lower-energy isotopes (e.g. ^{3}H, ^{14}C, ^{35}S) and soft gamma-emitters (e.g. ^{125}I and ^{99m}Tc) (Rapkin, 2001). The spatial resolution for emulsion is excellent for these same isotopes.

The advantage of autoradiography is that it is inexpensive. However, it is time consuming. Hence, over the past 15 years, phosphor-imaging has become a commonly used method of measuring radioactivity in tissue sections.

In phosphor-imaging, a reusable plastic sheet (storage phosphor screen) is used instead of film. The screen stores incident beta energy. After exposure, the screen is read digitally with a laser scanner and the ground state of the screen restored so that the screen can be reused.

For energetic beta-emitters, phosphor-imaging is approximately 10 times faster than either film or emulsion. However, phosphor imaging has several disadvantages: 1) tritium is not measurable without special and costly screens; 2) resolution is less than film; 3) because of the S-shaped response curve, exposures that are too long or short must be repeated. But more linear than film; 4) phosphor plates are expensive – from hundreds to over a $1000 each; and 5)

4

phosphor plates have limited reusability as they become contaminated or develop latent images.

The days, weeks, or months between sample preparation and data interpretation are unacceptable. Also, the use of isotopes with a short half-life is not possible. The Micro-Imager, a recently developed real-time digital beta-imaging system, overcomes these problems. The Micro-Imager permits direct visualization of results as they are acquired, so that no exposure is too short. Results are obtained 10-20 times faster with Micro-imaging than phosphor-imaging, and 100-300 times faster than film and/or emulsion. For example, a three month tritium autoradiogram with film takes only 8 hours using the Micro-Imager. Dual labeling counting allows competitive receptor binding studies or studies of the distribution of two drugs concurrently administered. Counting response is linear over a dynamic range of 10^4, a range 100-1000 times greater than film. The resolution is 15 μm for ^{3}H. Hence, the advantages of the Micro-Imager for radioactivity imaging of tissue slices are: 1) speed; 2) accurate quantification; 3) wide dynamic range; 4) routine tritium counting; and 5) dual labeling.

1.3 Micro-Autoradiography

Micro-autoradiography provides a 2-D image of the location of the radiation source, whereas techniques such as PET and SPECT provide a 3-D localization of the radiation source. However, the resolution of micro-

5

autoradiography (on the order of a few μm) is much higher than PET or SPECT (Lu et al., 2001).

Micro-autoradiography, generally uses a nuclear emulsion coating over labeled tissue sections. The tissue section may either be stained prior to or after the application of the emulsion coating (Rogers, 1979). The section is subsequently examined with a microscope (Young and Kuhar, 1979). It allows visualizing the localization of radiolabeled material at the cellular level in histological preparations.

There have been limited previous studies of 3-D reconstructed serial section autoradiographs or phosphor images (Roberson et al., 1992; Mohr et al., 2004; Hess et al., 1998; Yoshioka et al., 2000). However, the actual distributions of the radiolabels relative to the cellular histology in 3-D have not been well characterized. The goal of this project was to determine whether a novel micro-autoradiographic technique can be used to characterize the distribution of radiolabels with respect to cellular histology in 3-D that can be used for research.

1.4 Advantages of Radiolabels

The use of radiolabeled ligands to determine the tissue distribution of receptors is termed in vivo receptor autoradiography if the ligand is administered into the circulation, and in vitro receptor autoradiography when radiolabeled ligands are applied directly to tissue sections (Yamamura et al., 1974; Young and Kuhar, 1979).

6

Our goal is to produce a series of labeled tissue sections through in vivo radiolabeling. In vivo labeling is less expensive than using fluorescent dyes or quantum dots in vivo. Another disadvantage of using fluorescent dyes is that they burn out quickly (Service, 1998). Many radiolabels have a long half-life. For example, ^{3}H has a half-life of 12.28 years. Although quantum dots can fluoresce for weeks or longer, their disadvantage is their size. They are about 10 times bigger than most organic dyes (Seydel, 2003) and may not permeate cell membranes. In vitro labeling of tissue, by radiolabels, fluorescent dyes or quantum dots, that has already been sectioned is very time consuming, especially for a large number of sections (Tribollet et al., 2004). It is faster to inject a live animal with a radiolabel and then take tissue sections, e.g. brain sections.

1.5 Difficulties with Micro-Autoradiography Versus Digital Micro-Autoradiography

In traditional micro-autoradiography, a tissue section on a glass slide is manually dipped in emulsion, and left for an exposure period of two or more weeks - after which time the tissue sections are developed. However, the standard deviation in the variation in the mean grain count densities for 10 sections from the same tissue sample can vary from 6-34% (Humm et al., 1995). These variations were attributed principally to the variations in the sensitivity of the emulsion across the slide. As digital micro-autoradiography does not use emulsions, these difficulties will not arise.

7

1.6 Micro-Imaging

The Micro-Imager (Biospace Mesures, Paris, France) offers a digital solution to micro-autoradiography (Debruyne et al., 2005; Crumeyrolle-Arias et al., 2003; Langlois et al., 2001 ; Cloez-Tayarani et al., 1997). The Micro-Imager can be used to quantify the spatial distribution of radiolabels in a tissue. The Micro-Imager is based on the work of Georges Charpak for which he was awarded a Nobel Prize in Physics in 1992 (Charpak et al., 1989). The Micro-Imager uses a scintillation counting technique and sophisticated analysis of each individual decay event to determine location and intensity (Laniece et al., 1994; Dausse et al., 1995). The advantage of the Micro-Imager over autoradiography is the savings in time. The Micro-Imager produces results 100-300 times faster than film (Rapkin, 2001). Another advantage is that the Micro-Imager allows for <u>dual label</u> measurement, with tritium being one of the two labels. Hence, the Micro-Imager permits studies of the distribution of two drugs concurrently administered (Laniece et al., 1998; Salin et al., 2002). The Micro-Imager is well-suited to detect ligand receptors (Gautier and Bernand, 2001).

The Micro-Imager's file formats for exporting autoradiographic and optical images are available as jpeg, tiff, bmp and txt files.

1.7 Autoradiographic/Histological Image Fusion

Autoradiographic and optical images obtained from the Micro-Imager are already aligned (or registered). We plan to use commercially available imaging

8

software, MCID v.7.0 (InterFocus Imaging Ltd, UK), to align a shrunken version of the histological montage image to the optical image.

The tissue contours in the histological montage and the optical image are the same (as these are images of the same tissue section and not serial sections), so registering the two images can be done with the MCID v.7.0 registration function.

The registered montage image will then be enlarged and the associated registered autoradiograph will also be enlarged by the same scale. MCID v.7.0 will then be used to fuse the enlarged montage and autoradiogram together. MCID v.7.0 is compatible with the Micro-Imager's file format as it accepts and exports images in monochrome and color tiff. Image fusion can range from simple addition to weighted addition with layer-specific transparency. MCID also has editing features to remove artifacts. We will use a free 14 day trial version to illustrate an autoradiographic/histological fusion in our preliminary results described below.

1.8 Difficulties in 3-D Reconstruction of 2-D Micro-Autoradiographs

In theory, 3-D reconstruction of radiolabels at the cellular level from serial 2-D micro-autoradiographs requires alignment of the 2-D serial sections. However in practice, the alignment of serial tissue sections is very time consuming and labor-intensive. The number of slides can be on the order of hundreds (Lu et al., 2001; Manconi et al., 2001). Three-dimensional estimates of absorbed dose based on 2-D autoradiographs in internal radionuclides therapy

9

has been performed using a small number of sections (Lu et al., 2001). However, this mathematical estimation method cannot provide information with respect to the receptor distribution in the brain. We propose to improve the time consuming and labor-intensive process of 3-D reconstruction of 2-D micro-autoradiographs by using a combination of commercially available software.

1.9 Alignment of Serial 2-D Sections

As mentioned above the alignment of serial tissue sections is very time consuming and labor-intensive. We plan to use a semi-automatic process to align the fused montage/autoradiogram sections. The fused montage/autoradiogram sections will be reduced in size so that the brain shape can be seen. Alignment can be based on the shape of the tissue contour for course alignment, especially for tissue with well-defined external boundaries. Internal tissue features such as blood vessels, could be used to refine serial section alignment (Humm et al., 1995). In Manconi et al. (2001), an outline of the primary intrinsic structure can be made and put as an overlay on the next slide. They found that this technique provides a more precise registration than using fiduciary markers. Using the registration (or alignment) feature of MCID, all the sections will be aligned to the previous slide. These images will then be rendered as individual data sets in VoxBlast (see below).

10

1.10 3-D Rendering from 2-D Images

VoxBlast (Vaytek Inc., Fairfield, Iowa, USA) is a voxel-based 3-D volume rendering system developed by Randall Frank and maintained at the University of Iowa's Image Analysis Facility. VoxBlast creates 3-D projections from stacks of registered 2-D images. VoxBlast is measurement oriented. It is designed to let the user easily extract precise information from volumetric data. Some of its advantage include: multiple platform support; true 3-D analysis tools built into software; powerful built-in Palette editor for color and opacity definition; Brainvox tracing for correlating 3-D views with cross sectional views; and support tool including volumetric math calculations and image analysis. The most powerful tool is the transparency function, also called the opacity function. The transparency function allows the user to see through the whole object with areas of interest emphasized according to the desired results.

VoxBlast Light is available at no charge. VoxBlast Light is similar to VoxBlast except that measurement tools are not available. We will use VoxBlast Light to obtain our preliminary results with 3-D rendering as described below. VoxBlast Light now has expanded file-reading capability, including BioRad, Dicom, 8 and 16 bit TIFF, 8 and 16 bit TIFF multi-image, and 8 or 16 bit raw. Hence, both VoxBlast and VoxBlast Light will be able to create 3-D renderings from the exported files from MCID v.7.0 above.

The VoxBlast 3-D rendering software was successfully used to develop high resolution 3-D images using parallel histological serial sections displaying

11

microvascular and glandular structures in human endometrium (Manconi et al., 2001).

1.11 Micro-Autoradiographic Fusion Tomography (MAFT)

Three-dimensional micro-autoradiography is difficult to achieve because of the time and labor cost involved. We plan to reduce both time and labor by using digital micro-autoradiographic images obtained from the Micro-Imager along with commercially available software – MCID v.7.0 and VoxBlast. The MCID v.7.0 software together with VoxBlast provides an example of a computer visualization system that is capable of excellent 3-dimensional reconstruction from serially sectioned material for scientific interpretation and measurement purposes.

MAFT is unique as it provides high resolution of both the radiolabel and the cellular structure in 3-D. MAFT is a novel technique that will provide important new medical information such as in the investigation of receptor distribution in the brain, and the radiation absorbed dose to cells in tissue from radiopharmaceuticals used for therapy.

Chapter 2
Materials and Methods

2.1 Chemicals

[^{14}C]-Formaldehyde (40-60 mCi/mmol, 1-3% aqueous solution, 0.1 mCi/ml), was obtained from American Radio-labeled Chemicals (St. Louis, MO). Recombinant human vascular endothelial growth factor, (VEGF$_{165}$, carrier-free) was obtained from PeproTech (Rocky Hill, NJ). ScintiSafe Econo 1 liquid scintillation cocktail for radioactive sample counting was from Thermo Fisher Scientific (Pittsburgh, PA). All other chemicals and reagents were from Sigma-Aldrich (St. Louis, MO).

2.2 VEGF Radiolabeling

VEGF was radio-labeled via reductive methylation using a procedure modified from Kim and Burgess (Burgess et al., 2002). The reaction mixture consisted of 20 µg of VEGF dissolved in 0.19 ml deionized water, 0.1 ml of 0.2 M HEPES (pH 7.4) containing 0.01 M nickel chloride and 0.05 ml (5 µCi) of [^{14}C]-formaldehyde. The reaction was initiated at room temperature by the addition of 0.01 ml of freshly prepared 0.15 M sodium cyanoborohydride, followed by further incubation at 4°C for 20 h. The reaction mixture was transferred to dialysis tubing (SpectrPor, 0.32 ml/cm, 12,000-14,000 MWCO; Spectrum Laboratories, Rancho Dominguez, CA), and dialyzed at 4°C against 0.9% w/v sodium chloride for 48 h

13

(two changes of 500 ml). An aliquot (~6000 cpm) of the recovered [^{14}C]-VEGF was precipitated with trichloroacetic acid (TCA precipitation assay, ref – Goding, below) which showed that ~98% of the radioactivity precipitated as protein. Prior to animal injections, 200 µg of rat serum albumin (RSA) was added to the sample (10:1 w/w ratio of RSA to [^{14}C]-VEGF), and the sample was concentrated at room temperature to ~0.085 ml in a centrifugal filtration unit (Microcon YM-10, 10,000 MWCO; Millipore, Billerica, MA) spun at 12,000 x g. Almost 100% of the radioactivity loaded into the filtration unit was recovered in the retentate.

2.3 Subcutaneous Injection

Experiments were approved by the University of South Florida Animal Care and Use Program. Rats (Sprague Dawley, male, 375-399 g; Harlan, Indianapolis, IN), were anesthetized with 2% isoflurane in medical oxygen prior to injection. For the 2.5 minute experiment, [^{14}C]-VEGF (40 µl containing ~80,000 cpm; ~10 µg VEGF) was injected into the subcutaneous tissue on the shaved back of the rat using an insulin syringe equipped with a ½ inch, 28 gauge needle. The approximate duration of the injection was one second. The center of the injection site was marked with an indelible pen. After 2.5 min, a full thickness skin sample (14 mm x 14 mm x ~5 mm depth) containing the injection site was excised, placed into a plastic tissue mold (#03020; Surgipath Medical Industries, Eagle River, WI) and frozen on dry ice to immobilize the [^{14}C]-VEGF in the tissue.

2.4 Histological Processing

The frozen tissue samples were bisected transversely through the injection site and mounted on a cryostat chuck using embedding medium. For each tissue sample, ten consecutive, 10 μm-thick sections were cut in the transverse plane starting from the center of the injection site and mounted onto microscope slides. Sections were desiccated at -20°C until dry, and stored at room temperature with desiccant until imaging.

Distribution of radioactivity within the tissue sections was obtained using quantitative digital autoradiography on a Micro-Imager (Biospace Mesures, Paris, France). Each slide was imaged with a five hour exposure, thereby creating a black and white representation of the drug dispersal. The Micro-Imager is also capable of saving a black and white optical image which has the same spatial orientations as the autoradiographic figure, which will later be used to set image registration.

Tissue features within the section are then made visibly evident thru the use of a sample stain. In this case, hematoxylin and eosin (H&E) stain was applied. This allowed for details to be more apparent when optically imaged in a microscope using QCapture Pro.

2.5 Sizing Using QCapture Pro

A key part to allowing all of the following operations to commence is that the sizing and scale of each image must be equal. The autoradiographic images were saved with the dimensions of 1476 pi. X 1190 pi., where as the registered

15

black and white optical images were saved as 720 pi. X 581 pi. This adjustment simply requires that the optical image be expanded to the size of the autoradiographic image. After the sections have been stained, the sample must be re-imaged using a microscope with a color camera. This means that these images will be neither sized, scaled, nor oriented the same as the autoradiograph, and adjusted registered optical picture. The color images were sized 1024pi. X 768 pi., but they could not be simply resized like the black and white images. Instead, a size relation had to be found for an object in the pictures. Using the "ruler" tool in QCapture Pro, a measurement was taken between the same two points on both the black and white registered image and the color image. For this work, the color image had to be shrunk by a factor of 62% for the scales to be the same.

2.6 Alignment Using MCID

In order to combine the color and autoradiographic images, it is important to have them properly aligned. There is not enough detail in the autoradiographic picture to be able to find any identifiable landmarks with which to orient the color image. However, the black and white images are registered to the autoradiographic images by the nature of how they were created. Using the MCID Analysis software (InterFocus Imaging Ltd, Cambridge, England) the color images are rotated and translated so that they are properly registered. This is performed using the "Image Registration" tool which is a built in function of the program. A series of coincident points, three or more, are selected on both the

16

registered black and white image and the color microscopic image. The software is then able to determine the rotation and translation which best brings these points together. This is performed by the computer assuming that the images are "rigid," in that it will not deform either image to force the points to coincide. The general equation for this type of transformation takes the form of:

$$x' = R * x + t \qquad\qquad (1)$$

$$y' = R * y + t \qquad\qquad (2)$$

Where **R** is an orthogonal matrix which represents the rotation required based upon the chosen points. The **t** value is a vector which refers to the amount and direction of translation calculated.

2.7 Fusion Using MCID

Once the color and autoradiographic images have been registered, they can be combined or "fused." This basically entails one image being laid over another. In this instance, the autoradiographic images are placed over the color images, due to the fact that there is far more information present in the color pictures. This function is also performed using the MCID Analysis software, and is highly automated; only requiring the operator to load the two images to be fused. The output of this operation is a single new image which is saved and then re-registered to each other for the 3-D rendering.

17

2.8 3-D Rendering Using VoxBlast

The serial fused images are now ready to be run in the volume rendering program called VoxBlast (Vaytek, Fairfield, Iowa). This program is capable of taking a series of flat, two dimensional slides, and interpolating what the three dimensional solid looks like by using a number of selectable algorithms. This program then allows the user to adjust their viewpoint around, and thru the object. Another important tool incorporated with this program is a feature which allows the operator to essentially filter out any unwanted colors, leaving, for instance, only the color which represents the autoradiographic portion of the images.

18

Chapter 3
Results

3.1 Micro-Imager

Ten samples spaced 10 µm apart were collected via the procedures in chapter 2. The slides must first be processed via the Micro-Imager due to the fact that the procedure of slide staining will wash out the radioactivity. As was stated above, the Micro-Imager is capable of imaging both the autoradiographic picture, as well as a registered optical image in black and white. This can be seen be in Figure 1 below.
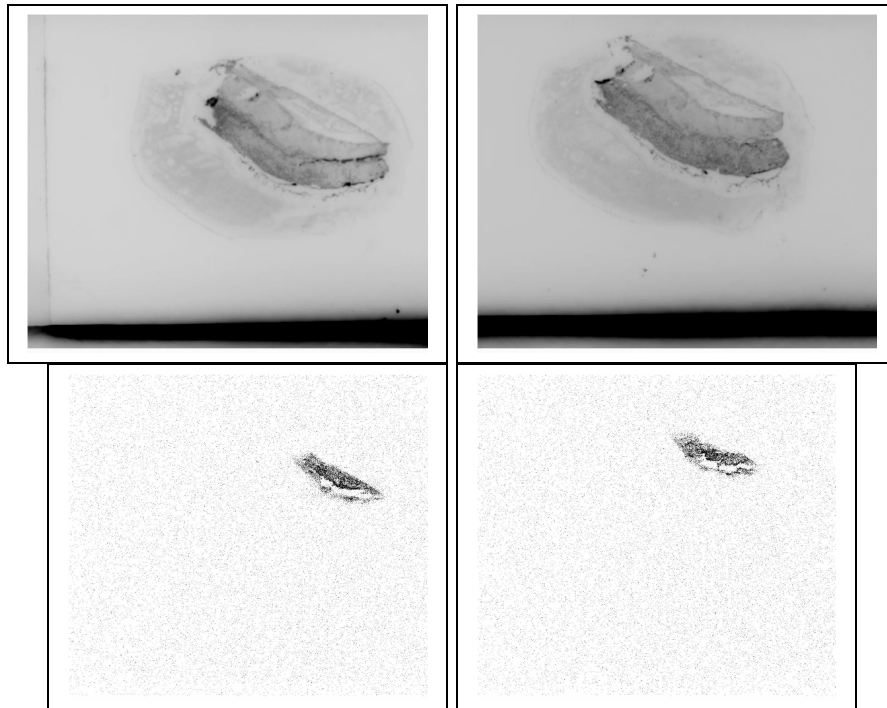

Figure 1. Optical (above) and autoradiographic (below) images of slides #1 and #2 respectively.

Very little detail can be seen with regard to the tissue types in the optical images, but they show enough of the outline that they can be used as references for the stained images which will be discussed next. If the autoradiographic image were to be overlaid upon the optical image, they would coincide completely as seen below, and this is what is meant by "registered" pictures. The autoradiographic data can be seen in green. This is why having the optical images is so important. There is almost no detail in the autoradiographic images which corresponds to any obvious feature in the optical image, and at least three are required to register an image.
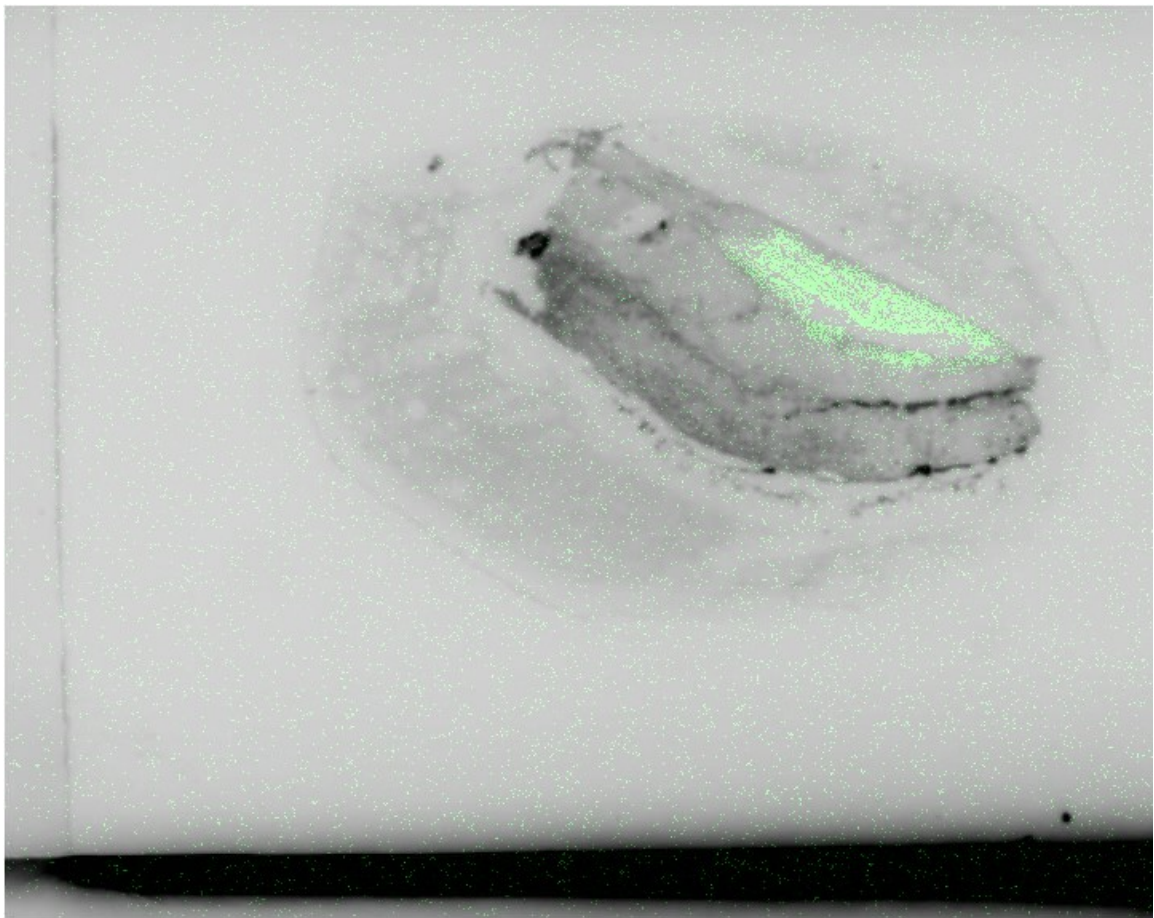

Figure 2. Fused optical and autoradiographic image.

3.2 Histological Processing

In Figure 3 can be seen the first three slides as imaged after the H&E stain has been applied. Upon close discrimination, it is apparent that these three images are quite similar, but they do have differences. Much of this is due to the changes in tissue between each slice. However, on the lower right quadrant of slide #2, a major discrepancy can be seen which is very much different from the sample on either side. This is due to a folding of the tissue as it was placed upon the slide. Such artifacts were only found on a couple of the slides, but this type of error is one which makes it difficult to later align the images for fusion.
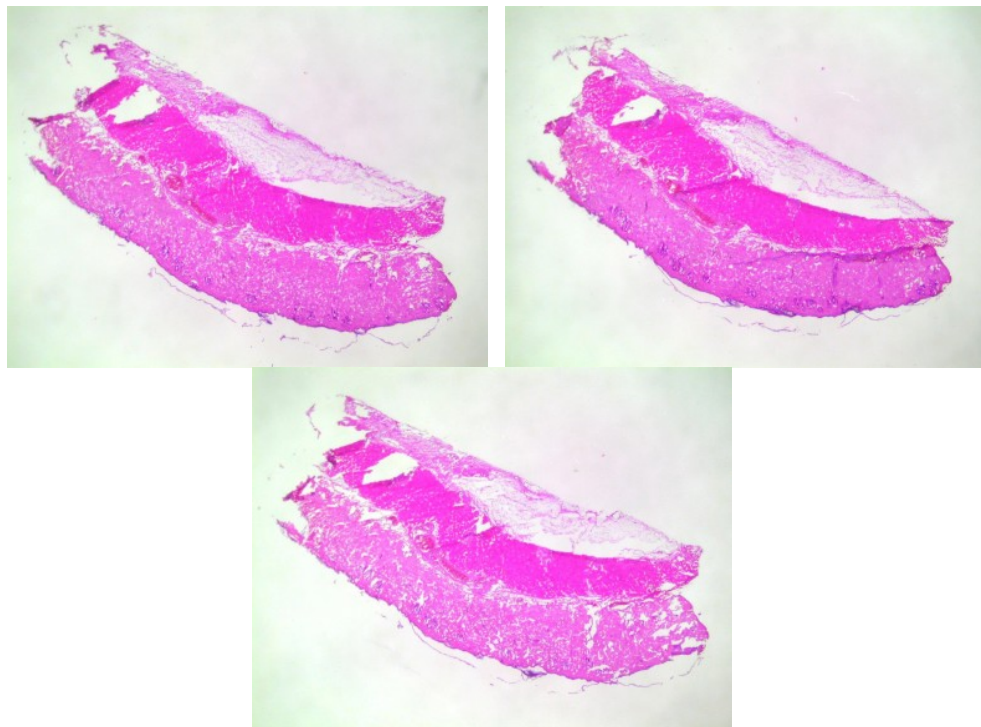

Figure 3. H&E stained slides #1, #2, and #3 respectively.

As compared to the images in Figure 1, there is much more information present to allow someone to identify tissue types. Had these slides not been

stained, very little detail would be evident to the naked eye. For instance, looking just left of center, a few blood vessels can be seen in a deeper red/purple. Depending upon the types of structures which are likely to be located in the samples, and what differentiations a researcher requires will determine the types of stains to be used.

3.3 Sizing Using QCapture Pro

All of the images shown in the sections above started out sized differently. In order to perform all of the following operations, it is very important that all of the images match in overall size and/or scale. The black and white optical and autoradiographic images were initially sized differently, but simply had to be made to be the same overall size. The fact that these images are already registered means that by sizing them the same, the scales will inherently be equal. The same cannot be said for the stained optical and the black and white optical images. As can be seen in Figure 3, a measurement tool had to be used to measure the number of pixels between two coincident points. Using the distances, a value for the percent reduction/enlargement can be found. For instance, in this study, the stained optical image had to be reduced to 38% of its original size.
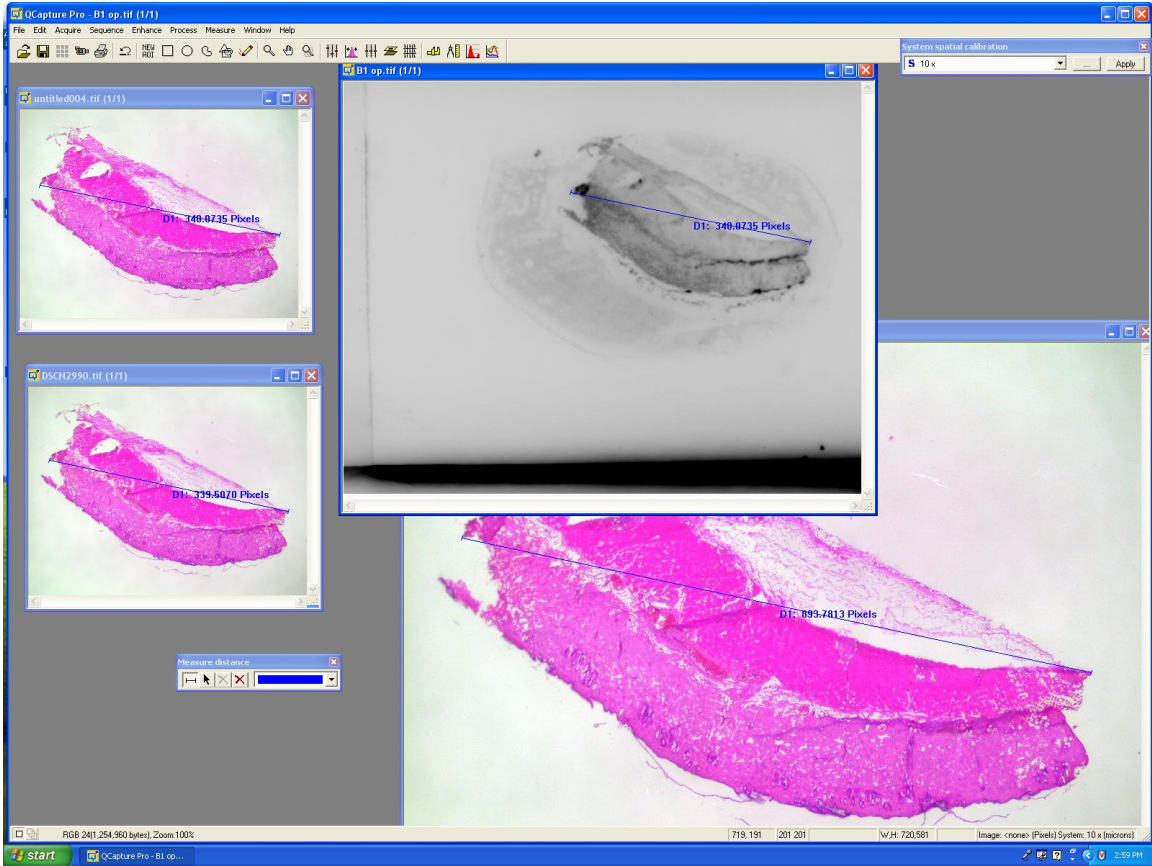
22

Figure 4. Screen shot of measurement tool in QCapture Pro.

3.4 Aligning Using MCID

In order to fuse the autoradiographic and stained images, they must first

be registered to one another. Due to the fact that there are no alignment marks

visible on the slide, the registration has to be done by hand. That means that the

operator must look at both images, and determine at least three points of

commonality, and then place a marker on each image.   This inherently

introduces a source of error, not to mention it is time consuming, but for these

intents and purposes, this is adequate. The MCID Analysis package does have

an alignment tool, which helps to stream line the process. In the future, it will be

23

worth spending more time learning about the functions within the software, and becoming capable of writing macros to perform much of this task.

The figure below shows the black and white optical image, as well as a registered stained image. Note that both the orientation and size are almost the same. The registered stained image below also shows better why the scales must be the same on all of the pictures. The white region with the pink specimen within is the stained image, and the surrounding black is an extended region which did not exist in that picture. That region was created by the computer so that the overall area of these two images is equal.
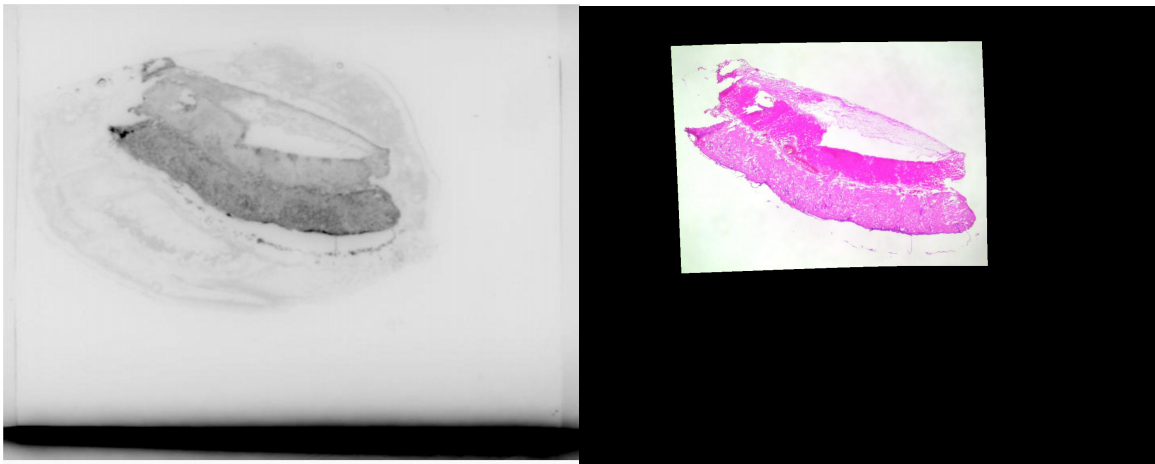

Figure 5. Black and white optical image and registered stained slide.

3.5 Fusion Using MCID

Once the images were aligned, as shown above, the newly registered stained image is ready to receive its autoradiographic overlay, or "fusion." This is one reason why MCID Analysis was chosen to work with. The fusion function is almost entirely automated. The operator simply needs to open the image which

will act as the underlaying and the overlaying image, in this case, the registered stained image and the autoradiographic image, respectively. It is important to recognize that the stained image is the underlayment because it contains more information. The autoradiograph is made up of a series of points which represent radiological events, and if properly exposed should have far less data than the stained image.
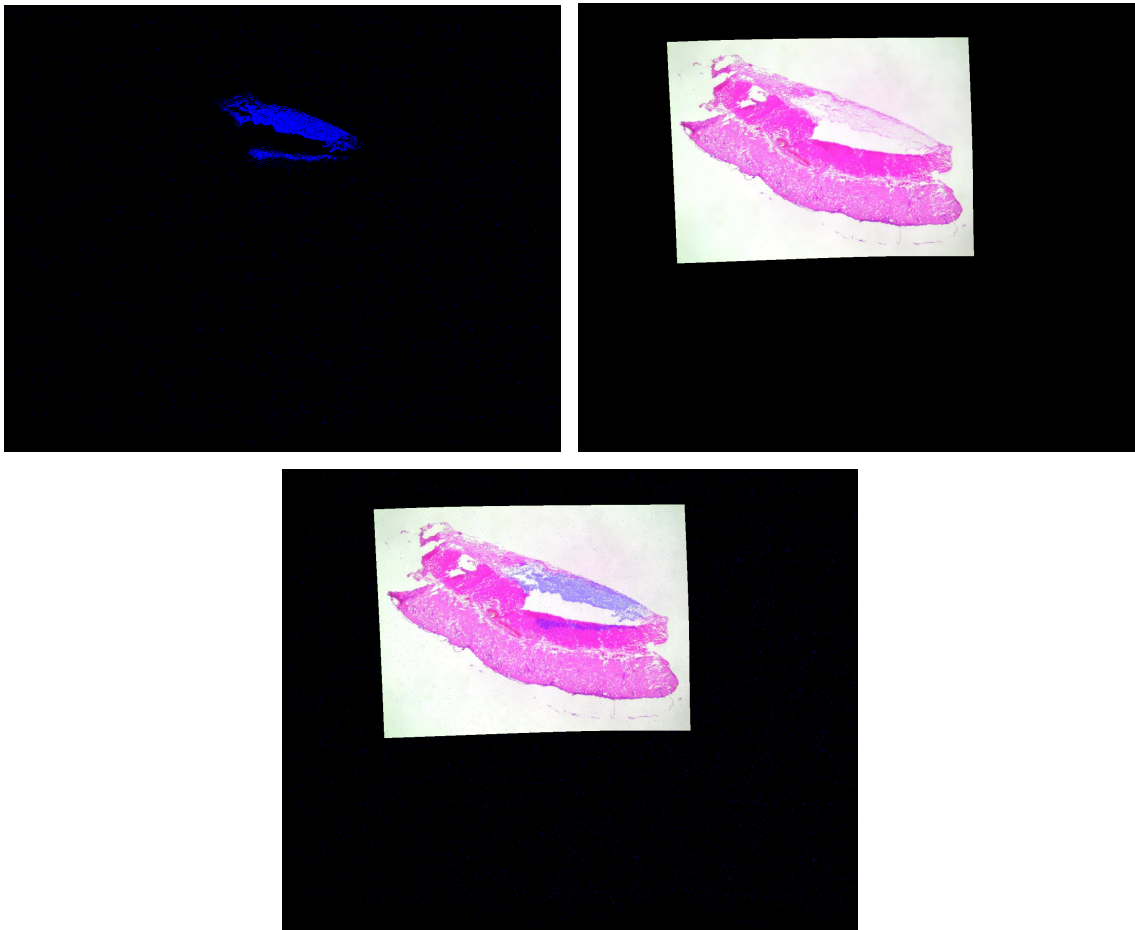

Figure 6. The autoradiograph (top left) is combined with the registered stained image (top right) to produce the fused image at the bottom.

3.6 3-D Rendering Using VoxBlast

Once the fused images are registered to each other, it is time to render them. VoxBlast makes this operation fairly easy, only requiring a few variables to be set and an indication where the images have been stored. Due to the fact that there were only ten consecutive slides to work with, the slide thicknesses were exaggerated so that a depth could be seen. The manufacture suggests not having the program interpolate more than 5 pixels deep for best clarity and reliability. This leads to equation 3 below, where T is the sample thickness, D_A is the actual distance measured, and D_I is the number of pixels making up that distance. The distances are measured with QCapture Pro, by looking at the microscopic view with a known calibrator.

$$T = 5 * (D_A / D_I) \tag{3}$$

One of the most significant tools in VoxBlast pertains to how it performs the rendering. Some of the algorithms allow for filters to be applied, so as to exaggerate or eradicate certain colors. This will prove to be quite useful when it comes to fused images. It enables the user to re-extract the autoradiographic date in three dimensions, and gain a better knowledge of the distribution in any plane. Figure 7 shows the ten slides set to be viewed as a solid, and Figure 8 shows the rendering with some of the background tissue filtered out to accentuate the blood vessels.
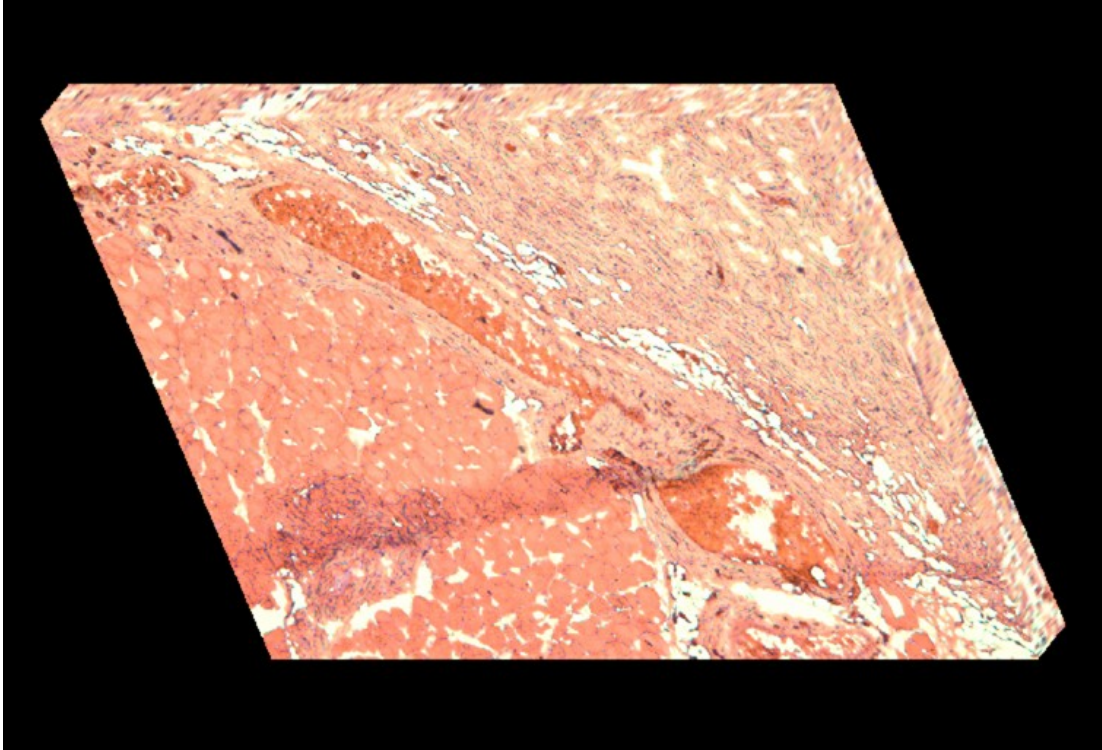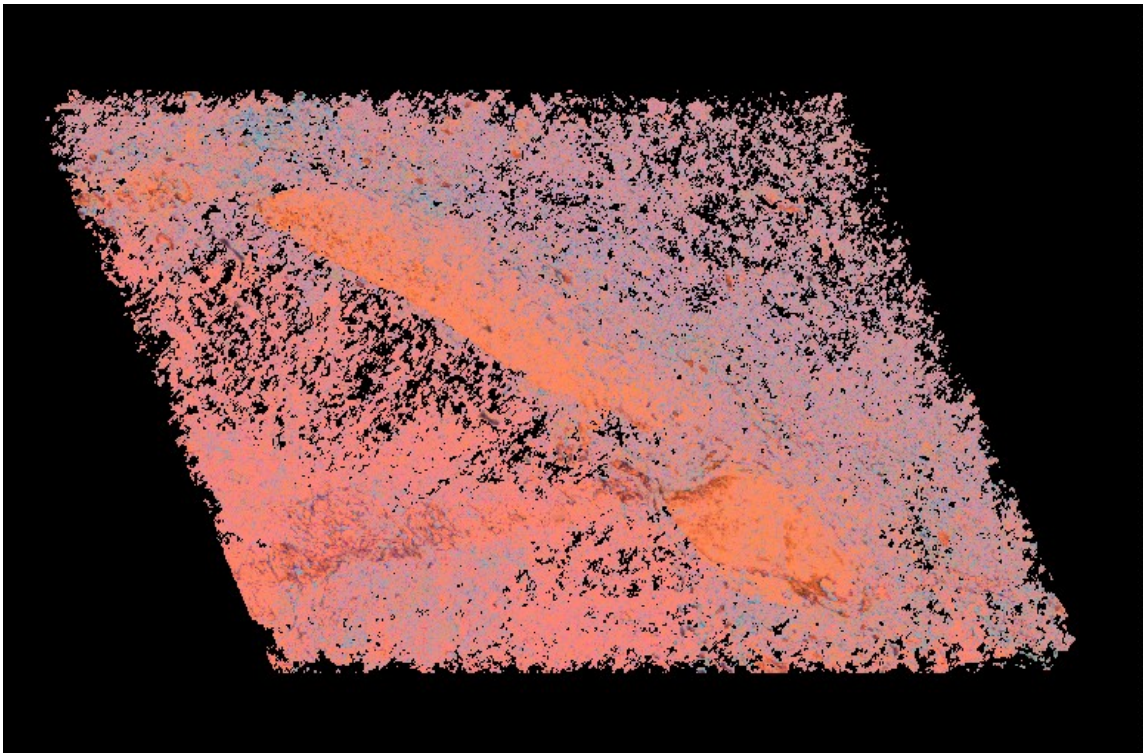
26

Figure 7. 3-D rendering of slides as a solid.

Figure 8. 3-D rendering of slides with some background filtered out.

27

Another useful part of this program deals with the creation of animations automatically. Much of the details can be much more easily discerned as the rendering is rotated. VoxBlast has some pre-designed movie "script" built into the system, but it isn't difficult to write custom scripts to more readily show any fine points. Unfortunately, movies cannot be shown in a report, so the true power of this software package is not easy to demonstrate.

In the Figure below can be seen the user interface, which consists of three primary windows: control panel, status window, and the rendering window. The control panel is where most of the setup and adjustment is done. The status window shows what the program is currently doing, and can be used as a command prompt rather than using the graphical interface of the control panel. The rendering window works just as it sounds, it displays the current rendering as is set by the control panel or command prompt. In Figure 8, there is a fourth window open on the lower left of the screen shot, this is the color palette tool, which is used in conjunction with the various algorithms to accentuate or negate certain colors.
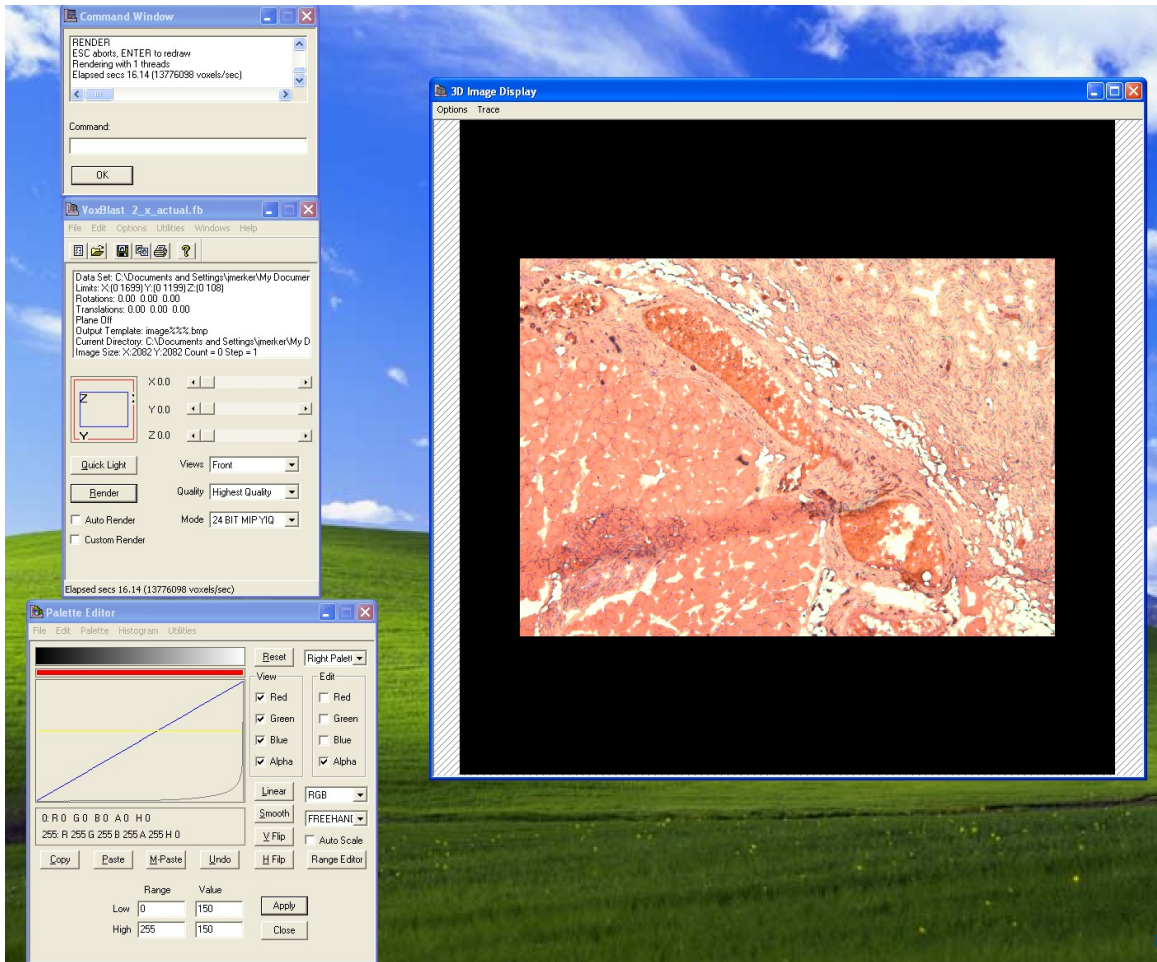
28

Figure 9. Screen shot of the VoxBlast user interface.

Chapter 4
Discussion

4.1 Histological Processing

When preparing a sample to be sectioned, it is very important that the thickness be appropriate. As can be seen in Figure 10, as the interpolated areas between the slide become larger, small spots and point begin to stretch over the gap, which turns something which should look round into a cylindrical shape. This distortion is easily remedied before the slices are cut. Vaytek recommends that a spacing of no more than five pixels be used. This means that the user needs to determine the appropriate scale (µm/pixel) for what they intend to investigate, and multiply it by 5 pixels to determine the maximum thickness for each section. This means that the optimum resolution for the slides which were worked with would have been 2 µm/pixel.

Figure 10. Side view of 3-D rendered solid.

30

Another important consideration pertains to the stain used after the autoradiography. It is apparent that the purpose of a stain is to allow ease of identification to structures within a tissue sample. However, it is also important to keep in mind that the autoradiographic image must also be easy to extract after the fusion has taken place. This means that if a stain is used which will exhibit every color of the rainbow, it will be very difficult to filter that out later without loosing pertinent data about the radioactivity.

4.2 Sizing and Alignment

The sizing and alignment of the slides is critical to making everything happen. None of these software packages can perform their various tasks meaningfully with out the proper registration and scaling. This is also the most time consuming part at present. It is apparent that should MAFT be used on a larger scale, this portion must be made automatic. This is the beauty of the MCID Analysis software. It has the ability to run "macro" programs within its framework. A macro can be used to identify markers which are frozen vertically along side the sample. These markers would essentially act as guides to allow a program which can identify them, and use them not only as registration marks, but as references to account for some inaccuracies incurred during the slicing and mounting of specimen.

31

4.3 Fusion Using MCID

The process of image fusion is actually quite simple to perform. As with many things, the devil is in the details. The work done with the sizing and alignment of the slides will determine the quality of the outcome. Another important detail which must be worked out before this stage is what color to use for the autoradiographic image. It is imperative that a distinct color be chosen which is not present in the stained image. If this were not done, false readings could be picked up, or the radiographic data may be lost as a result of the filtering process.

4.4 3-D Rendering Using VoxBlast

As with the fusion of images, it is very important that the alignment of the images be fairly close. This is another reason why having an automated process which can handle the majority of the monotonous job of aligning the images is so desirable. The process of rendering the image is very straight forward, as can be seen in Appendix B. The finesse comes into play as the operator determines the best algorithm to be used, and adjusts the color palette to negate the background image. This research project is limited to only operating with the basic filters and algorithms due to the shear amount of power which is housed within both VoxBlast and MCID Analysis. Using 3-D rendering, in combination with the cutting plane tool also found in VoxBlast, will allow an unprecedented view into what is happening in multiple planes within a test specimen.

32

Chapter 5
Conclusion

5.1 MAFT

Micro-autoradiographic fusion tomography (MAFT) is, and will be, an incredibly useful tool at the disposal of researchers. Micro-autoradiographs are often of little use without the context contained within cellular level optical images.   MAFT allows for that context to be re-combined with the autoradiographs and for it to then be added or subtracted at will. Far more viable data can be garnered for the dispersal characteristics of radiolabeled drugs and substances in this manner, as compared to current standards. Instead of being limited to the extent of the 2-D slides which are created, a close approximation to the sample can be created virtually and then re-cut in any orientation desired to better characterize drug diffusions. Due to that fact that the autoradiographs are done using the digital Micro-Imager, there is a much quicker turn around rate and inherently less labor required as compared with traditional micro-autoradiography. This application of MAFT has one further benefit of being performed with commercially available products, which means that it is available to a much more vast audience than a code which has to be created for each institution or research group.

5.2 Future Work

Although MAFT will be a great tool at the disposal of researchers, it still requires much refining to cut down on the amount of labor required to perform all of the intermediate tasks. The most significant and time consuming part of the process described above pertains to the preliminary alignment for image fusion, as well as the secondary alignment need for VoxBlast. Fortunately, this aspect also shows the most promise for improvement, with the implementation of only a couple improvements.

One potential area to investigate pertains to the methodology of the freezing and sectioning of samples. If, after the sample has been frozen, some sort of artificial marker is implanted within the block, yet away from the sample, which would allow for registration marks to be present on each slide, the registration process will be vastly improved. These marks will need to be marked with a radiolabel, as well as be visible with a microscope. Once the slides have been read and loaded into the MCID Analysis software, each image will only need to be registered once, and the need for the user to identify useful coincident points will have been eliminated.

A second aspect to be looked into deals with the advanced properties of the MCID Analysis package. This program allows for the creation of sub-programs, called macros, which could be created to perform the tasks of registration, as well as fusion. The MCID software uses its own language to call upon various components, and will likely require an engineer to learn it. Once

34

this subroutine is created, it should be easily modified to work with a host of different sample sizes and types.

35

References

Adriani W, Macri S, Pacifici R, Laviola G. (2002) Peculiar vulnerability to nicotine oral self-administration in mice during early adolescence. Neuropsychopharmacology. 27(2):212-224.

Adriani W, Granstrem O, Macri S, Izykenova G, Dambinova S, Laviola G. (2004) Behavioral and neurochemical vulnerability during adolescence in mice: studies with nicotine. Neuropsychopharmacology. 29(5):869-78.

Aine CJ. (1995). A conceptual overview and critique of functional neuroimaging techniques in humans: I. MRI/fMRI and PET. Crit Rev Neurobiol 9(2-3):229-309.

Atweh SF, Kuhar MJ. (1977a). Autoradiographic localization of opiate receptors in rat brain. I. Spinal cord and lower medulla. Brain Research. 124:53-67.

Atweh SF, Kuhar MJ. (1977b). Autoradiographic localization of opiate receptors in rat brain. II. The brain stem. Brain Research. 129:1-12.

Belluzzi JD, Wang R, Leslie FM. (2005). Acetaldehyde enhances acquisition of nicotine self-administration in adolescent rats. Neuropsychopharmacology. 30(4):705-712.

Benwell MEM, Balfour DJK, Anderson JM. (1988). Evidence that tobacco smoking increases the density of (-)-[^{3}H]nicotine binding sites in human brain. J Neurochem. 50:1243-1247.

Burgess DJ, Kim TK. Pharmacokinetic characterization of 14C-vascular endothelial growth factor controlled release microspheres using a rat model. *J Pharm Pharmacol*. (2002) 54:897-905.

Budinger TF. Positron-Emission Tomography (PET). In The Biomedical Engineering Handbook, 2nd ed; Bronzino JD, Ed.; CRC Press: Boca Raton, 2000; Vol 1, 67:7-17.

Chambers RA, Taylor JR, Potenza MN. (2003) Developmental neurocircuitry of motivation in adolescence: a critical period of addiction vulnerability. Am J Psychiatry 160(6):1041-1052.

36

Charpak G, Dominik W, Zaganidis N. (1989). Optical imaging of the spatial distribution of β-particles emerging from surfaces. Proc. Natl. Acad. Sci. 86:1741-1745.

Clarke PB. (1990). Mesolimbic dopamine activation--the key to nicotine reinforcement? Ciba Found Symp. 152:153-62; discussion 162-168.

Cloez-Tayarani I, Cardona A, Rousselle J-C, Massot O, Edelman L, Fillion G. (1997). Autoradiographic characterization of [^{3}H]-5-HT-moduline binding sites in rodent brain and their relationship to 5-HT$_{1B}$ receptors. Proc. Natl. Acad. Sci. Neurobiology. 94:9899-9904.

Connolly S, Macovski A, Pauly J. Magnetic Resonance Imaging. In The Biomedical Engineering Handbook, 2nd ed; Bronzino JD, Ed.; CRC Press: Boca Raton, 2000; Vol 1, 63:1-9.

Crumeyrolle-Arias M, Medvedev A, Cardona A, Barritault D, Glover V. (2003). In situ imaging of specific binding of [^{3}H]isatin in rat brain. Journal of Neurochemistry. 84:618-620.

Cunningham IA. Computed Tomography. In The Biomedical Engineering Handbook, 2nd ed; Bronzino JD, Ed.; CRC Press: Boca Raton, 2000; Vol 1, 62:1-13.

Dausse E, Quemeneur E, Schwartz K. (1995). ^{33}P and β-Imager: Application for genotyping of microsatellite markers. Biotechniques. 18(3):426-8,430.

Debruyne D, Quentin T, Poisnel G, Lelong-Boulouard V, Barre L, Coquerel A. (2005). Acute and chronic administration of clorazepate modifies the cell surface regulation of μ opioid receptors induced by buprenorphine in specific regions of the rat brain. Brain Research. 1052:222-231.

Dursun SM, Reveley MA. (1997). Differential effects of transdermal nicotine on microstructured analyses of tics in Tourette's syndrome: an open study. Psychol Med. 27(2):483-7.

Flores CM, Rogers SW, Pabreza LA, Wolfe BB, Kellar KJ. (1992). A subtype of nicotinic cholinergeric receptor in rat brain is composed of α4 and β2 subunits and is up-regulated by chronic nicotine treatment. Mol Pharmacol. 41:31-37.

Gautier B, Bernand BA. (2001). On the use of the Micro-Imager to directly visualize drug distribution in human skin. Skin Pharmacol Appl Skin Physiol. 14(suppl 1):41-45.

Griffith MH, Yorke ED, Wessels BW, DeNardo GL, Neacy WP. (1988). Direct dose confirmation of quantitative autoradiography with micro-TLD measurements for radioimmunotherapy. J Nucl Med. 29:1795-1809.

Grunwald F, Schrock H, Theilen H, Biber A, Kuschinsky W. (1988). Local cerebral glucose utilization of the awake rat during chronic administration of nicotine. Brain Res. 26;456(2):350-356.

Hess A, Lohmann K, Gundelfinger ED, Scheich H. (1998). A new method for reliable and efficient reconstruction of 3-dimensional images from autoradiographs of brain sections. Journal of Neuroscience Methods. 84:77-86.

Humm JL, Macklis RM, Lu XQ, Yang Y, Bump K, Beresford, Chin LM. (1995). The spatial accuracy of cellular dose estimates obtained from 3-D reconstruction serial tissue autoradiographs. Phys Med Biol. 40:163-180.

Koral KF, Kwok CS, Yang FE, Brown RS, Sisson JC, Wahl RL. (1993). Autoradiography-based, three-dimensional calculation of dose rate for murine, human-tumor xenografts. Nucl Med Biol. 20(8):901-909.

Kwong KK, Chesler DA. Functional MRI. In The Biomedical Engineering Handbook, 2nd ed; Bronzino JD, Ed.; CRC Press: Boca Raton, 2000; Vol 1, 63.3:22-31.

Langlois X, Riele PT, Wintmolders C, Leysen JE, Jurzak M. (2001). Use of the β-Imager for rapid ex vivo autoradiography exemplified with central nervous system penetrating neurokinin 3 antagonists. JPET. 299:712-717.

Laniece P, Charon Y, Dumas S, Mastrippolito R, Pinot L, Tricoire H, Valentin L. (1994) HRRI: a high resolution radioimager for fast, direct quantification in in situ hybridization experiments. Biotechniques. 17(2):338-45.

Laniece P, Charon Y, Cardona A, Pinot L, Maitrejean S, Mastrippolito R, Sandkamp B, Valentin L. (1998). A new high resolution radioimager for the quantitative analysis of radiolabelled molecules in tissue section. Journal of Neuroscience Methods. 86:1-5.

Lapchak PA, Araujo DM, Quirion R, Collier B. (1989). Effect of chronic nicotine treatment on nicotinic autoreceptor function and N-[^{3}H]methylcarbamylcholine binding sites in the rat brain. J Neurochem. 52:483-491.

Lu XQ, Humm JL, Chin LM. (2001). Estimate of absorbed dose based on two-dimensional autoradiographic information in internal radionuclide therapy. Med Phys. 28(3):328-35.

Manconi F, Markham R, Cox G, Kable E, Fraser IS. (2001). Computer-generated, three-dimensional reconstruction of histological parallel serial sections displaying microvascular and glandular structures in human endometrium. Micron. 32:449-453.

Maskos U, Molles BE, Pons S, Besson M, Guiard BP, Guilloux JP, Evrard A, Cazala P, Cormier A, Mameli-Engvall M, Dufour N, Cloez-Tayarani I, Bemelmans AP, Mallet J, Gardier AM, David V, Faure P, Granon S, Changeux JP. (2005). Nicotine reinforcement and cognition restored by targeted expression of nicotinic receptors.Nature. 436(7047):103-107.

McGehee DS, Role LW. (1995). Physiological diversity of nicotinic acetylcholine receptors expressed by vertebrate neurons. Annu Rev Physiol. 57:521-546.

Mohr J, Hess A, Scholz M, Obermayer K. (2004). A method for the automatic segmentation of autoradiographic image stacks and spatial normalization of functional cortical activity patterns. Journal of Neuroscience Methods. 134:45-58.

Nakayama H, Nakashima T, Kurogochi Y. (1991). α-4 is a major acetylcholine binding subunit of cholinergic ligand affinity-purified nicotinic acetylcholine receptor from rat brains. Neurosci Lett. 121:122-124.

Newhouse PA, Potter A, Kelton M, Corwin J. (2001). Nicotinic treatment of Alzheimer's disease. Biol Psychiatry. 49(3):268-278.

Nordberg A, Romanelli L, Sundwall A, Bianchi C, Beani L. (1989). Effect of acute and subchronic nicotine treatment on cortical acetylcholine release and on nicotinic receptors in rats and guinea-pigs. Br J Pharmacol. 98:71-78.

Papke RL. (1993). The kinetic properties of neuronal nicotinic receptors: genetic basis of functional diversity. Prog Neurobiol. 41(4):509-531.

Picciotto MR, Zoli M, Changeux JP. (1999). Use of knock-out mice to determine the molecular basis for the actions of nicotine. Nicotine Tob Res. 1 Suppl 2:S121-5; discussion S139-40.

Potter A, Corwin J, Lang J, Piasecki M, Lenox R, Newhouse PA. (1999). Acute effects of the selective cholinergic channel activator (nicotinic agonist) ABT-418 in Alzheimer's disease. Psychopharmacology (Berl). 142(4):334-42.

Rapkin E. (2001). Real-time radioimaging of biological tissue sections. American Biotechnology Laboratory. 19:34-36.

Roberson PL, Buchsbaum DJ, Heidorn DB, Haken R.K.T. (1992). Three-dimensional tumor dosimetry for radioimmunotherapy using serial autoradiography. International journal of radiation oncology, biology, physics. 24:329-334.

Roberson PL, Heidorn DB, Kessler ML, Haken RKT, Buchsbaum DJ. (1994). Three-dimensional reconstruction of monoclonal antibody uptake in tumor and calculation of beta dose-rate nonuniformity. Cancer. 73:912-918.

Rogers AW. (1979). Techniques of autoradiography, 3rd Edition. Elsevier North Holland.

Rosecrans JA, Stimler CA, Hendry JS, Meltzer LT. (1989). Nicotine-induced tolerance and dependence in rats and mice: studies involving schedule-controlled behavior. Prog Brain Res. 79:239-248.

Salin H, Vujasinovic T, Mazurie A, Maitrejean S, Menini C, Mallet J, Dumas S. (2002). A novel sensitive microarray approach for differential screening using probes labeled with two different radioelements. Nucleic acids research. 30(4):e17.

Salin-Pascual RJ. (2002). Relationship between mood improvement and sleep changes with acute nicotine administration in non-smoking major depressed patients. Rev Invest Clin. 54(1):36-40.

Salminen O, Murphy KL, McIntosh JM, Drago J, Marks MJ, Collins AC, Grady SR. (2004). Subunit composition and pharmacology of two classes of striatal presynaptic nicotinic acetylcholine receptors mediating dopamine release in mice. Mol Pharmacol. 65(6):1526-35.

Sanberg PR, Silver AA, Shytle RD, Philipp MK, Cahill DW, Fogelson HM, McConville BJ. (1997). Nicotine for the treatment of Tourette's syndrome. Pharmacol Ther. 74(1):21-25.

Schwartz RD, Kellar KJ. (1985). In vivo regulation of [^{3}H]-acetylcholine recognition sites in brain by nicotinic cholinergic drugs. J Neurochem. 45:427-433.

Service RF. (1998). Semiconductor beacons light up cell structures. Science. 281:1930-1931.

Seydel C. (2003). Quantum dots get wet. Science. 300:80-81.

Spear LP. (2000) The adolescent brain and age-related behavioral manifestations. Neuroscience and biobehavioral reviews. 24:417-463.

40

Stolerman IP, Reavill C. (1989). Primary cholinergic and indirect dopaminergic mediation of behavioral effects to nicotine, in Progress in Brain Research, Vol 29: Nicotinic Receptors in the CNS: Their Role in Synaptic Transmission (Nordberg A., Fuxe K, Holmstedt B, and Sundwall A., eds), pp. 227-237. Elsevier Science, Amsterdam.

Stolerman IP. (1990). Behavioral pharmacology of nicotine: implications for multiple brain nicotinic receptors. Ciba Found Symp. 152:3-16; discussion 16-22.

Tribollet E, Bertrand D, Marguerat A, Raggenbass M. (2004). Comparative distribution of nicotinic receptor subtypes during development, adulthood and aging: an autoradiographic study in the rat brain. Neuroscience. 124(2):405-420.

Tsui BMW. SPECT (Single-Photon Emission Computed Tomography). In The Biomedical Engineering Handbook, 2nd ed; Bronzino JD, Ed.; CRC Press: Boca Raton, 2000; Vol 1, 64:10-31.

Wada E, Wada K, Boulter J, Deneris E, Heinemann S, Patrick J, Swanson LW. (1989). Distribution of alpha2, alpha3, alpha4, and beta2 neuronal nicotinic receptor subunit mRNAs in the central nervous system: a hybridization histochemical study in the rat. J Comp Neurol. 284:314-335.

Weiller C, May A, Sach M, Buhmann C, Rijntjes M. (2006). Role of functional imaging in neurological disorders. Journal of magnetic resonance imaging. 23(6):840-850.

Whiting PJ, Schoepfer R, Conroy WG, Gore MJ, Keyer KT, Shimasaki S, Esch F, Lindstrom JM. (1991). Expression of nicotinic acetylcholine receptor subtypes in brain and retina. Mol Brain Res. 10:61-70.

Wilson AL, Langley LK, Monley J, Bauer T, Rottunda S, McFalls E, Kovera C, McCarten JR. (1995). Nicotine patches in Alzheimer's disease: pilot study on learning, memory, and safety. Pharmacol Biochem Behav. 51(2-3):509-514.

Yamamura HI, Kuhar MJ, Snyder SH. (1974). In vivo identification of muscarinic cholinergic receptor binding in rat brain. Brain Research. 80:170-176.

Yoshioka K, Gao D-W, Chin M, Stillson C, Penades E, Lesh M, O'Connell W, Dae M. (2000). Heterogeneous sympathetic innervation influences local myocardial repolarization in normally perfused rabbit hearts. Circulation. 101:1060-1066.

Young H, Baum R, Cremerius U, Herholz K, Hoekstra O, Lammertsma AA, Prium J, Price P. (1999). Measurement of clinical and subclinical tumor response using [18F]-fluorodeoxyglucose and positron emission tomography: review and 1999 EORTC recommendations. European Journal of Cancer. 35(13):1773-1782.

Young WS 3rd, Kuhar MJ. (1979). A new method for receptor autoradiography: [3H]opioid receptors in rat brain. Brain Res. 179(2):255-270.

Yu ZJ, Morgan DG, Wecker L. (1996). Distribution of three nicotinic receptor α4 mRNA Transcripts in rat brain: Selective regulation by nicotine administration. Journal of Neurochemistry. 66(3):1326-1329.

Appendices

Appendix A: MAFT Protocol

1) Using QCapture Pro, the black and white optical image acquired from the Micro-Imager and the stained optical image acquired from a microscope mounted camera is measured at two conspicuous points on the same slide using the "measure distance" function. These two values can be used to determine the factor of reduction/enlargement.
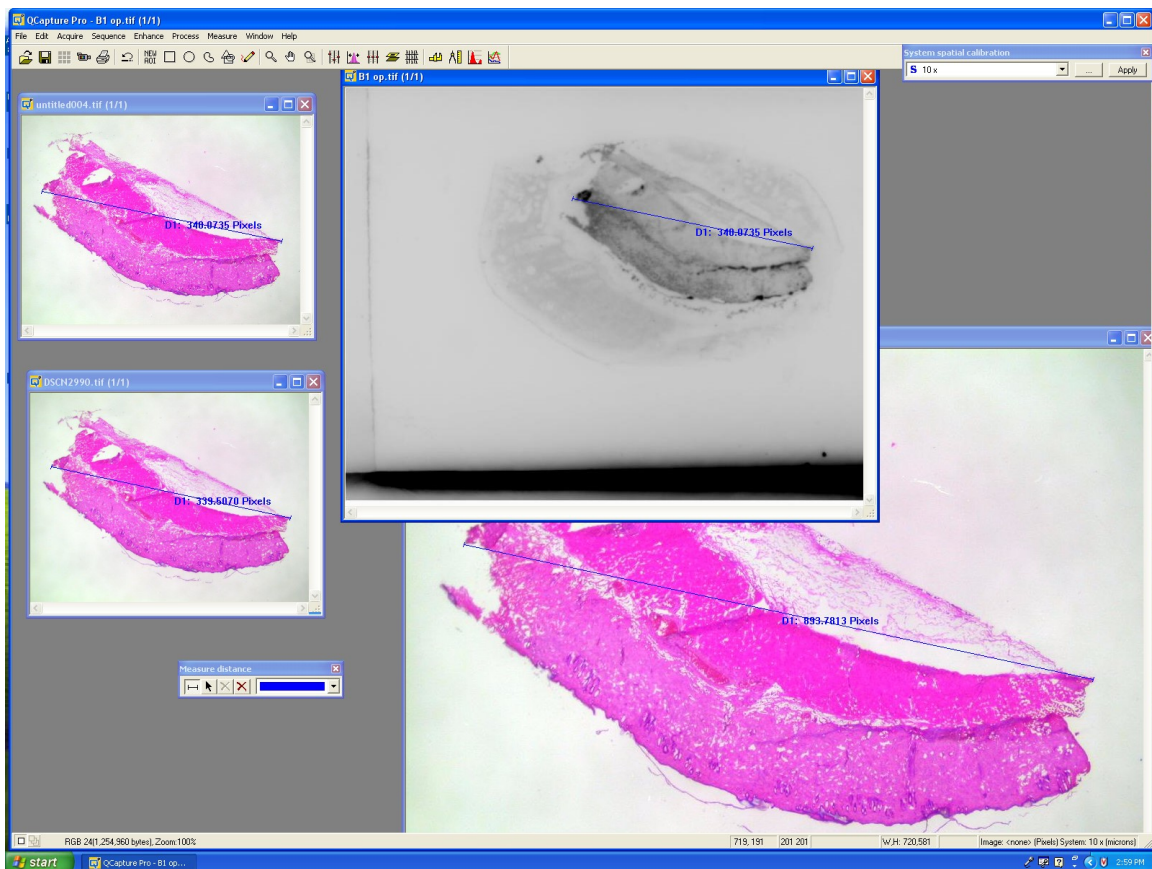
Figure 11. Measuring coincident points on a slide to determine the factor of reduction/enlargement.

2) Select the following commands: Edit >> Resize

3) Use the factor found above to adjust both the vertical and horizontal image size.

44

Appendix A: (Continued)

4) The stained optical image must now be registered to the black and white optical image. This task is performed with the MCID Analysis software package. The stained image is loaded into the channel 1 window, and the optical image is loaded into the channel 2 window. Then use the following commands to access the registration tool:

Transform (in operations tool bar on the left side of the screen) >>

Transform (top command line) >> Image Registration.
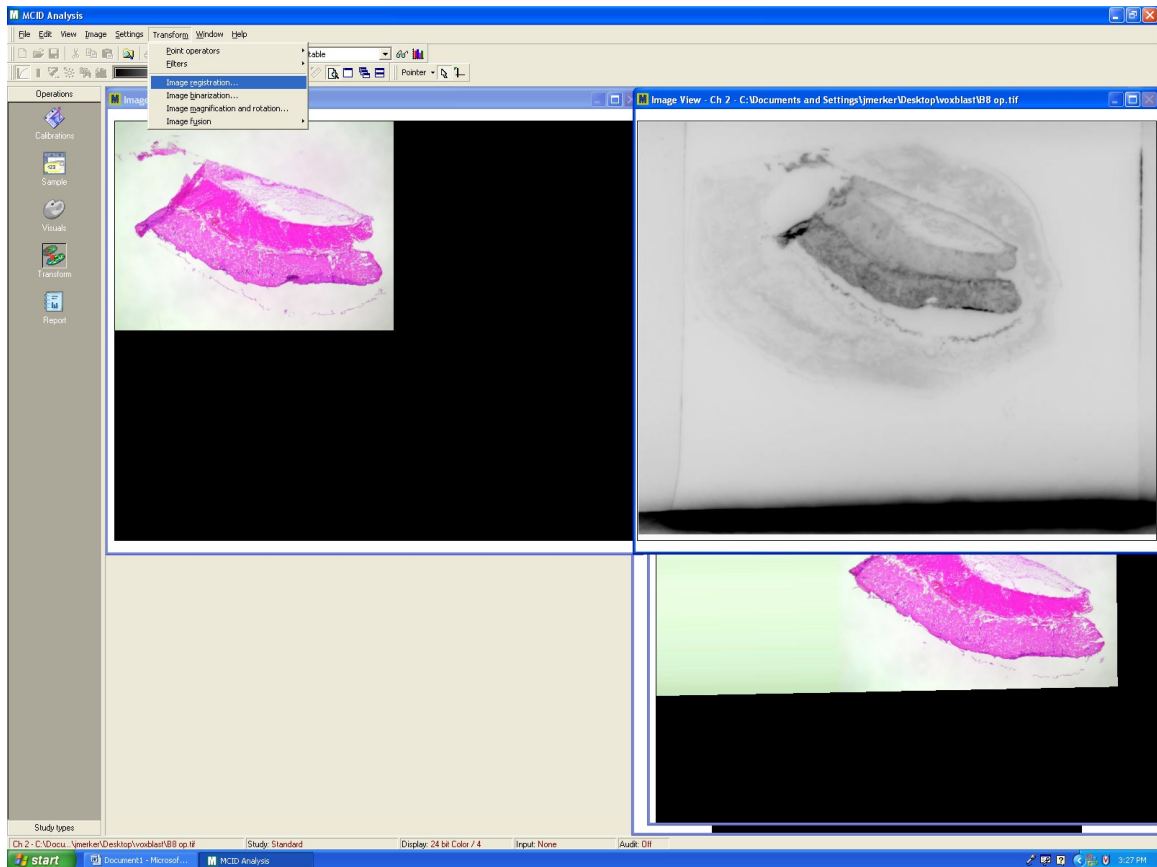
Figure 12. Loading the stained and optical images into the MCID Analysis software.

Appendix A: (Continued)

5) At least three coincident points must be chosen on each image, as shown below. The reference channel is the image which will not be changed by the registration process, and conversely the source channel is what will be changed. After the points have been aligned on each window, press "Apply," and save the output image in channel 3.
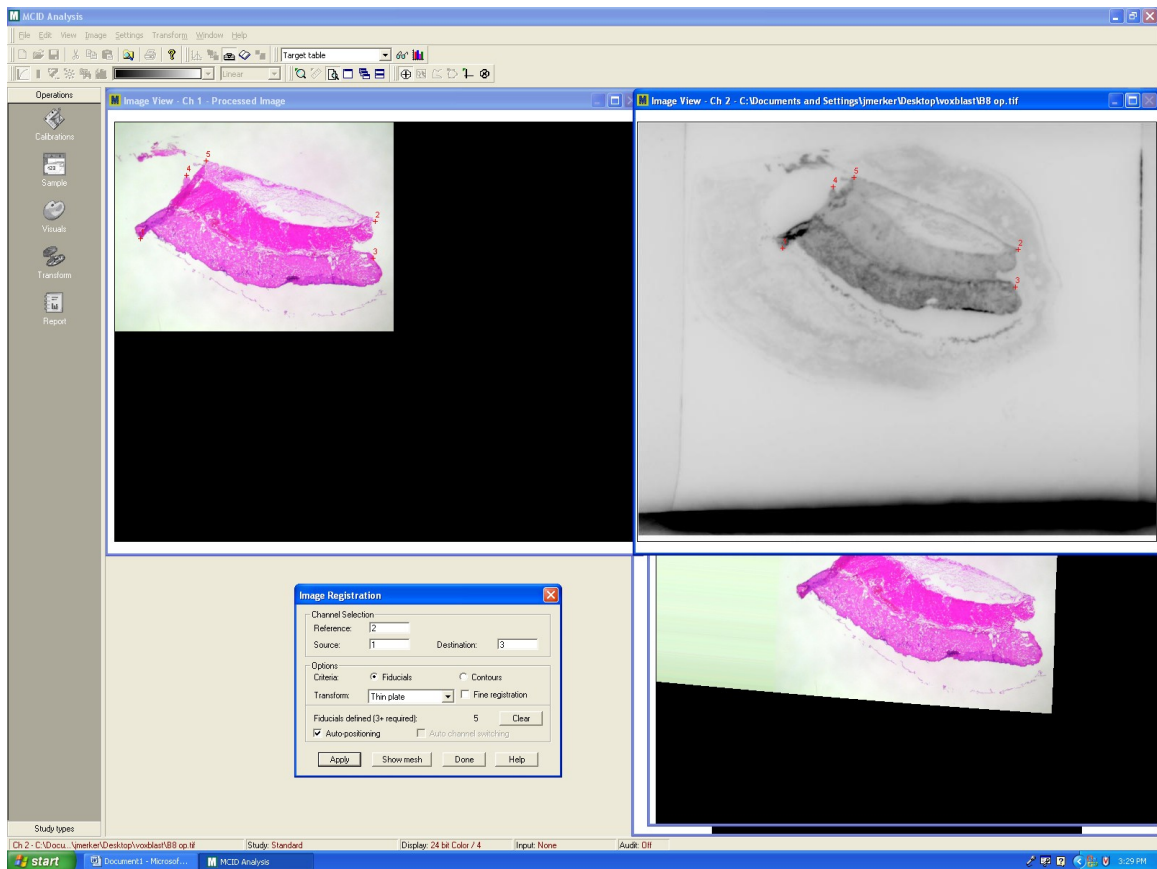
Figure 13. Choosing coincident points for image registration.

46

Appendix A: (Continued)

6) The gray-scale autoradiograph saved by the Micro-Imager must be converted so that the data can be differentiated from the stained optical image. This is accomplished using the QCapture Pro program. With the image loaded, use the following commands:

Edit >> Convert to >> Gray Scale 8

Process >> Pseudo-Color

7) An appropriate color scheme should be chosen and then the image must be converted back to a different format.

Edit >> Convert to >> RGB 24
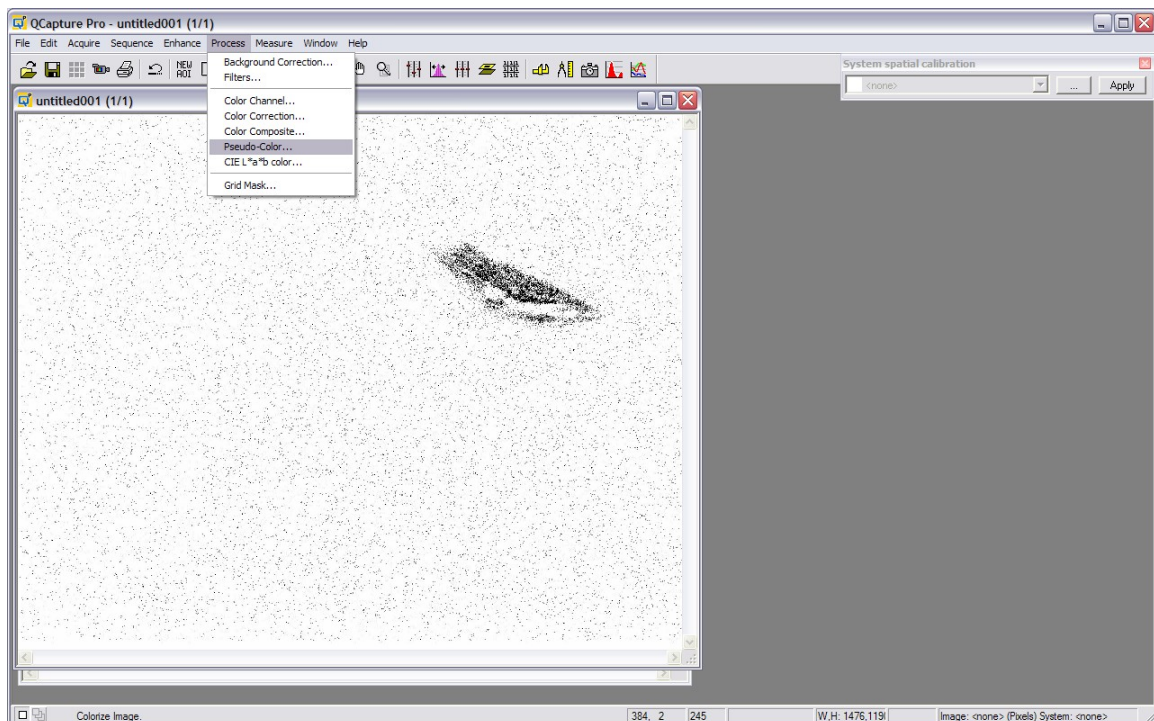
Figure 14. Giving the black and white autoradiograph some color.

Appendix A: (Continued)

8) It is now time to fuse the stained image with the autoradiograph. This is performed in the MCID Analysis program. The autoradiograph is loaded into channel 1, and the registered stained image is loaded into channel 2.

Transform >> Image fusion >> Basic

9) The start channel is selected to be 1, the end channel is 2, and the output will be loaded into channel 3. This image is then save, with the name being the same for all except for the last two or three digits. These must be numbers which increase by one for each file.
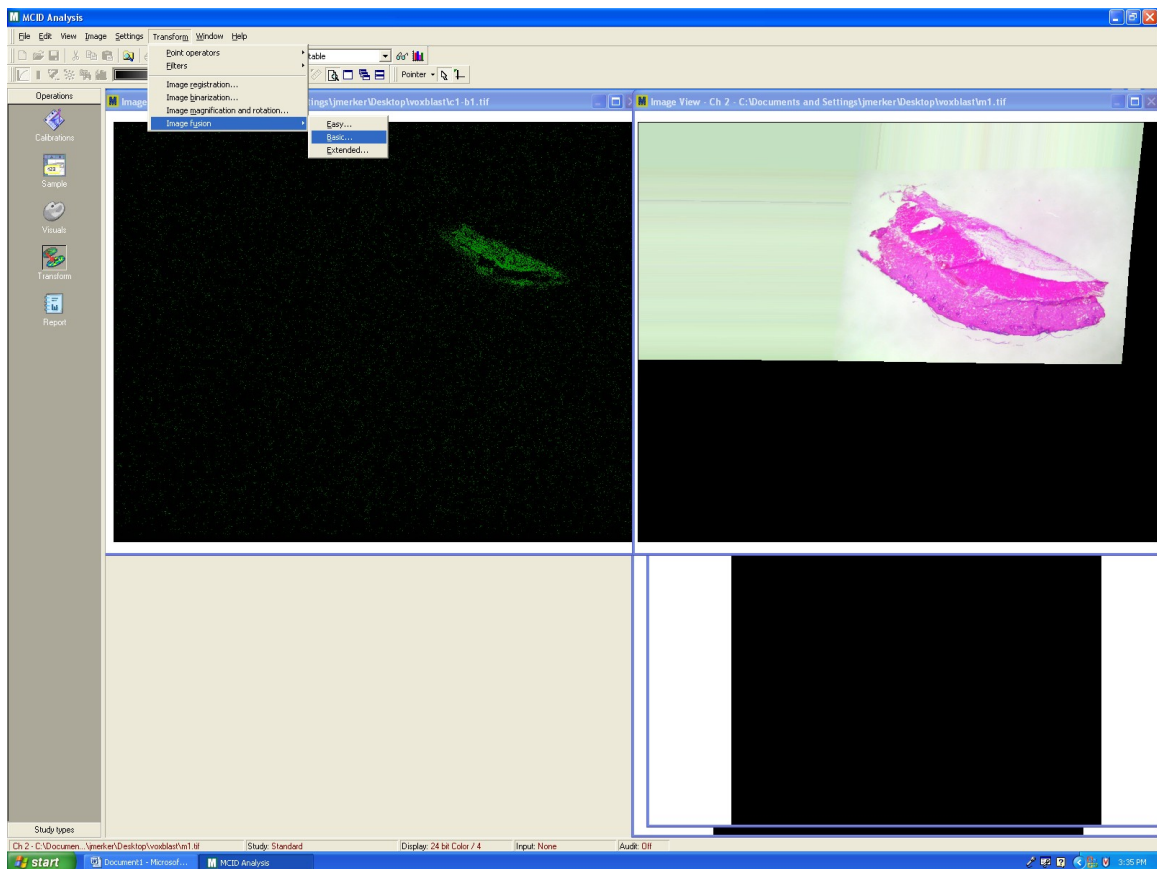
Figure 15. Accessing the image fusion tool in MCID Analysis.

Appendix A: (Continued)
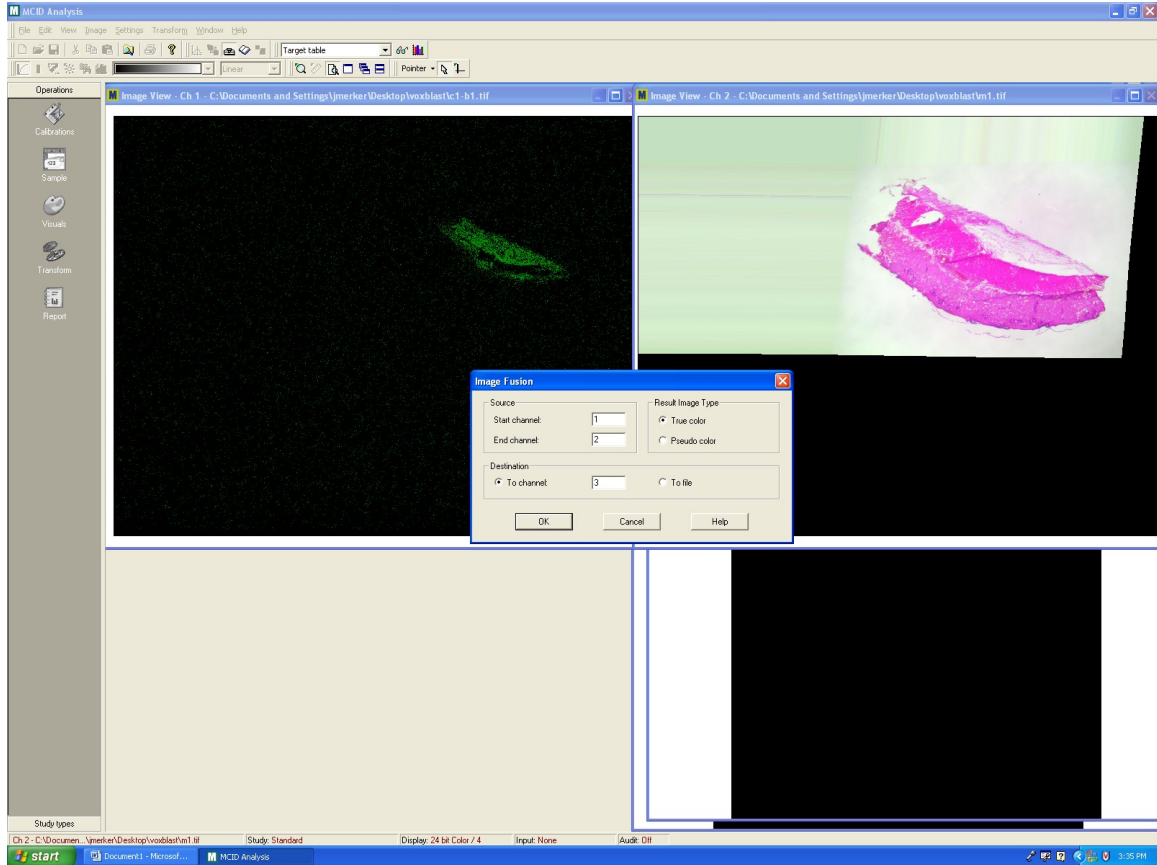
Figure 16. Setting up the fusion tool.

Appendix A: (Continued)

10) The images now need to be realigned with each other so that they can next be rendered using VoxBlast. The procedure is the same as above.

Transform (in operations tool bar on the left side of the screen) >>

Transform (top command line) >> Image Registration
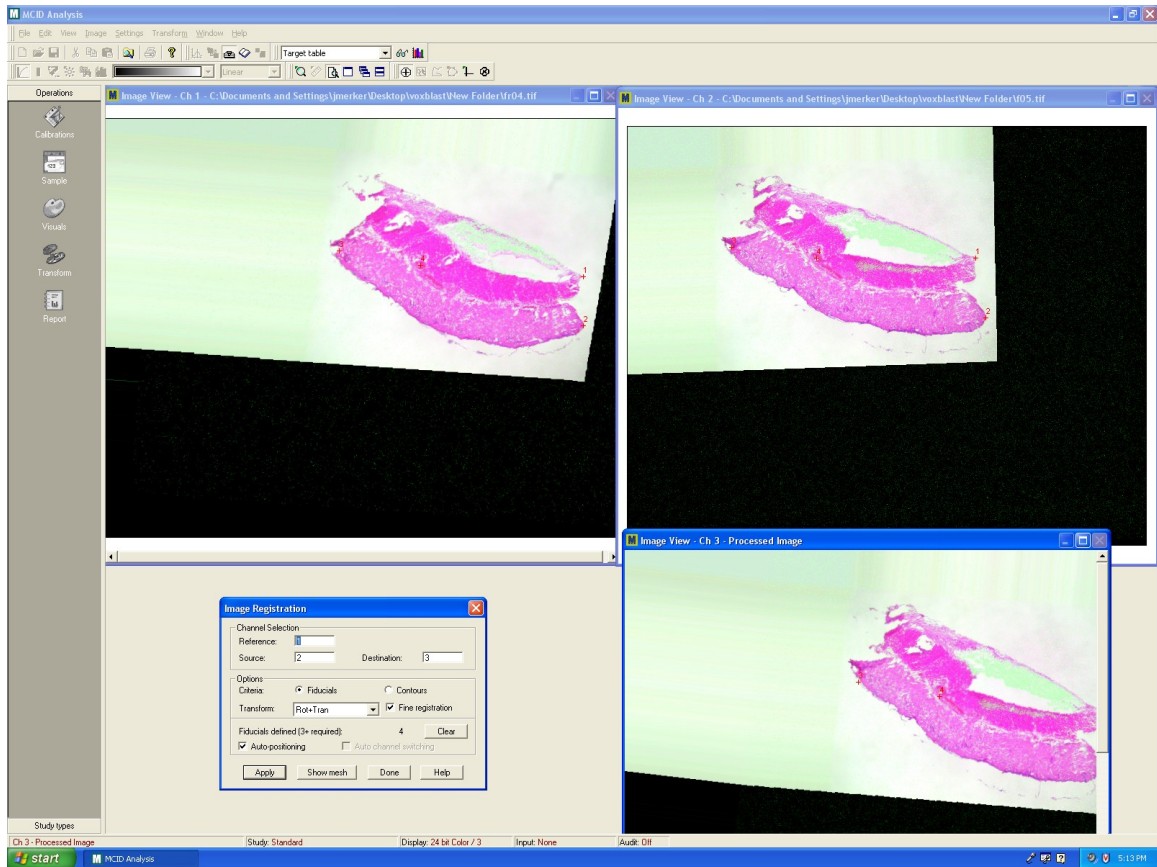
Figure 17. Registering the fused images.

Appendix A: (Continued)

11) The next step is to render the 3-D image using the series of slides which were just prepared. To load them: File >> New Dataset Definition.
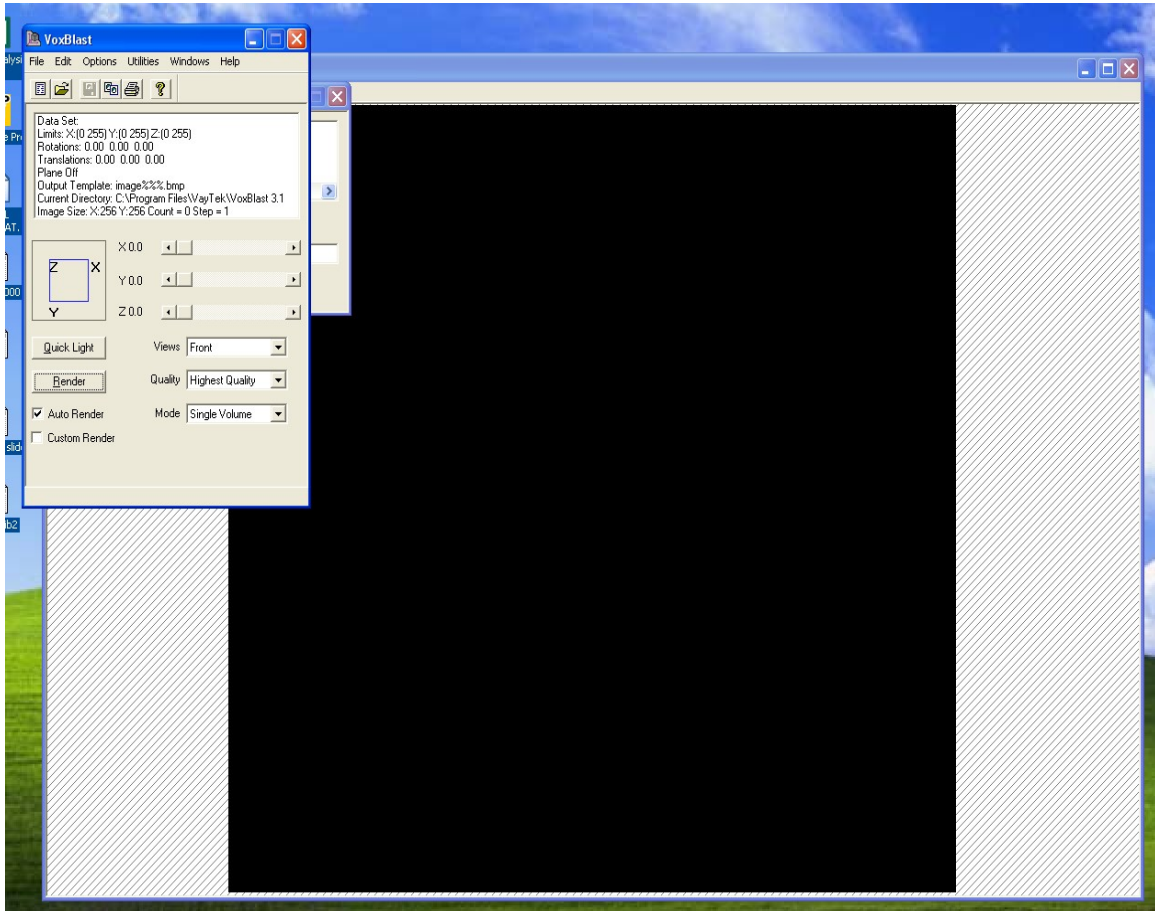
Figure 18. VoxBlast upon startup.

Appendix A: (Continued)
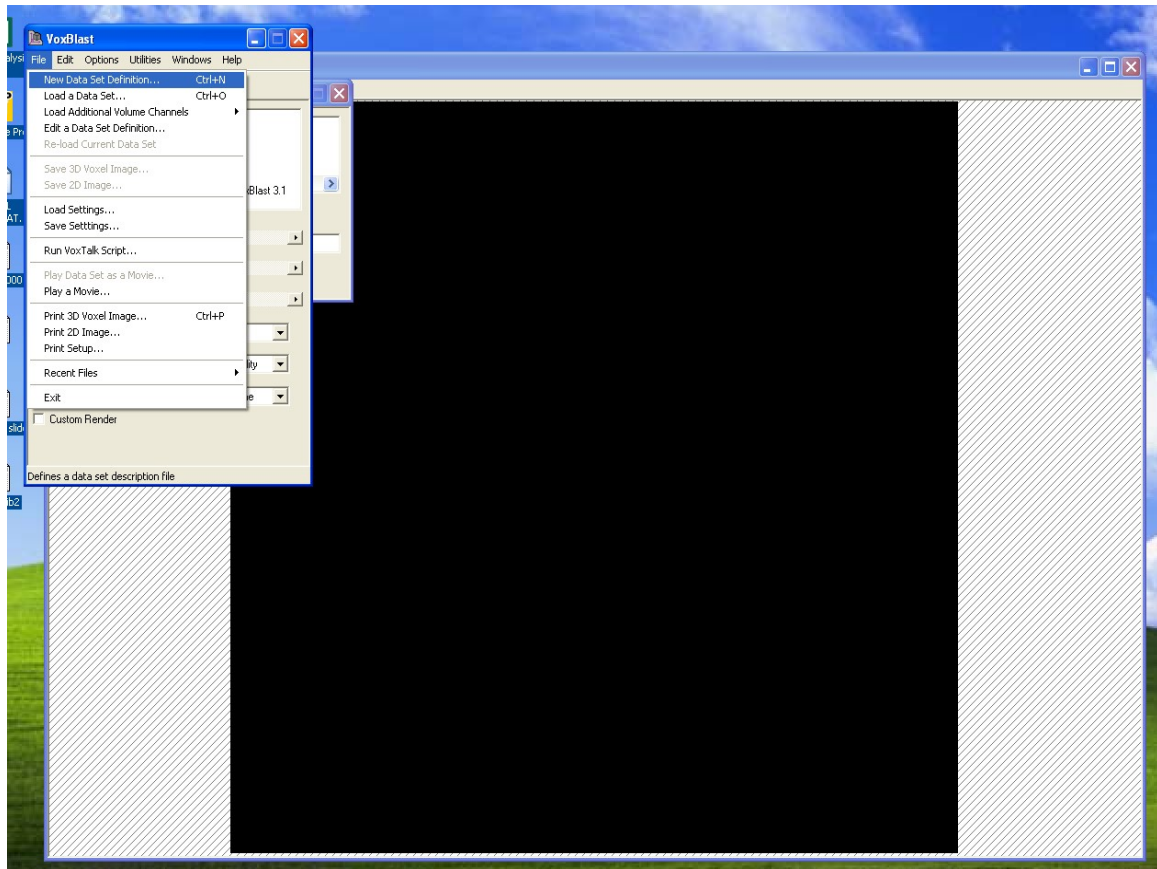
Figure 19. Commanding VoxBlast to open a new definition set.

Appendix A: (Continued)

12) In the Input Template field, a "%" is used to represent the part of the file names which are all the same. The easy way to create the template is by clicking on the "…" and selecting the first image. One will also have to put in the starting number, ending number and step size to allow VoxBlast to call up the pictures. The interpixel value is the size of on pixel, in μm for this instance. The interslice is the thickness between each section. These values can be changed at a later time without difficulty.
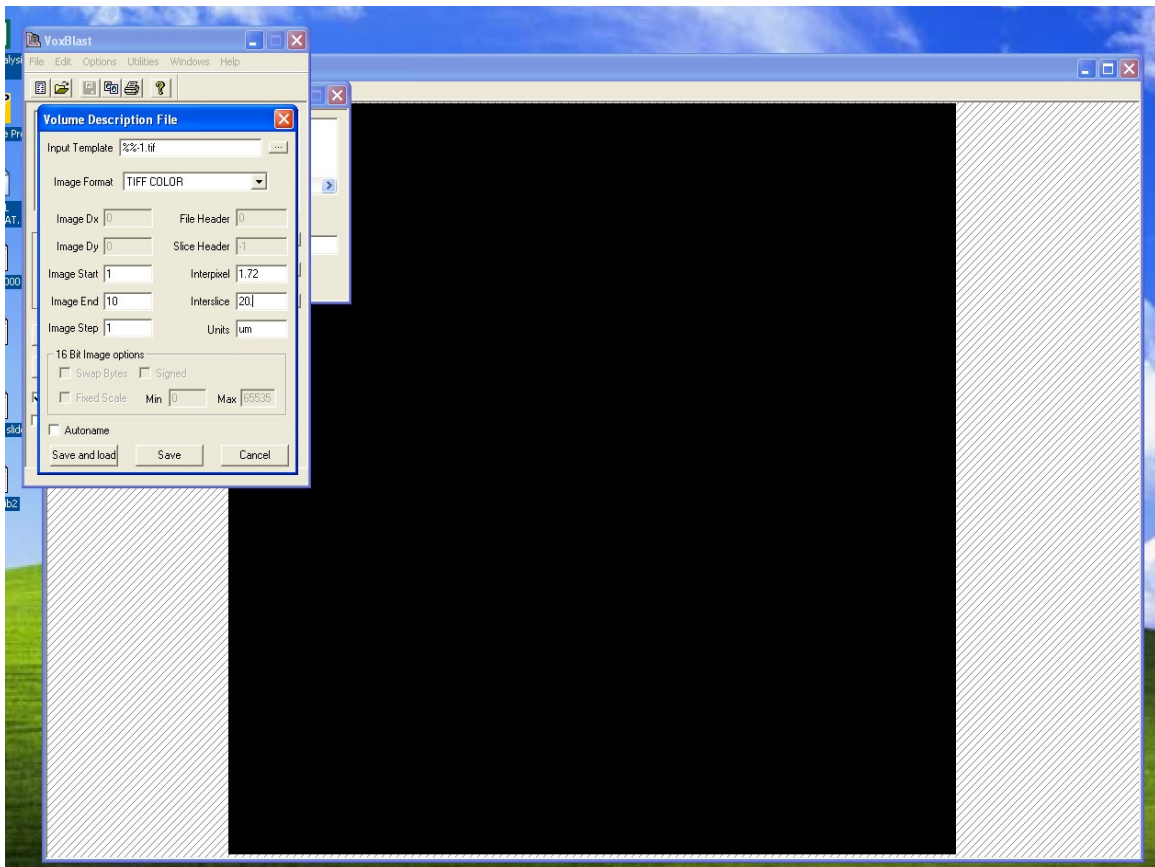
Figure 20. VoxBlast volume description window.

Appendix A: (Continued)
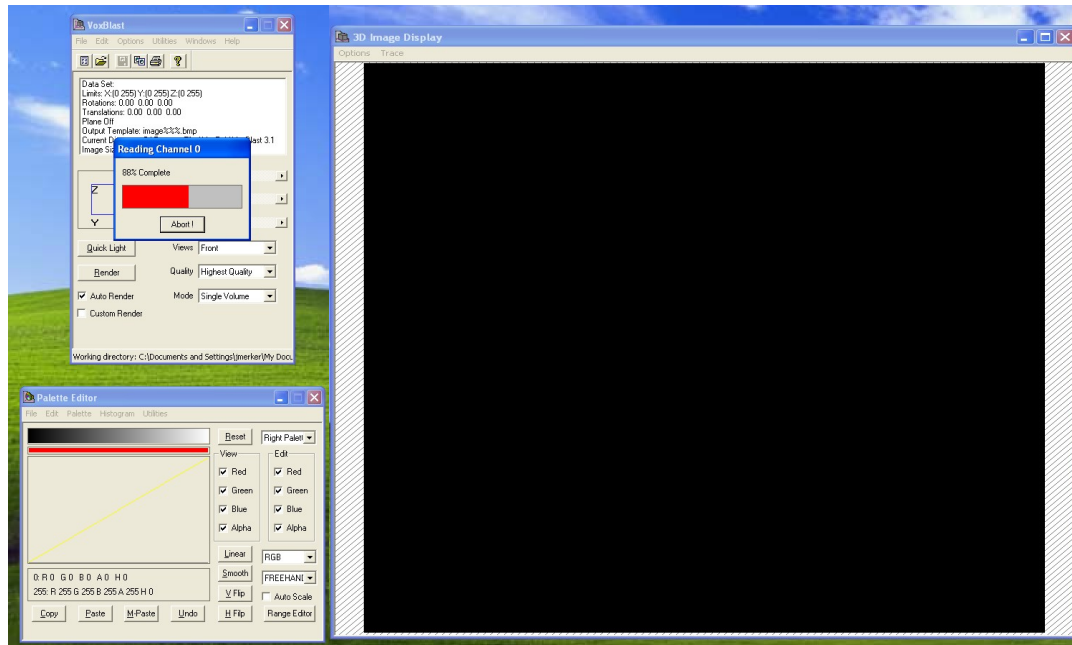
Figure 21. VoxBlast loading the data set.

Appendix A: (Continued)

13) It is now time to work with the various modes and filters to garner the desired results.
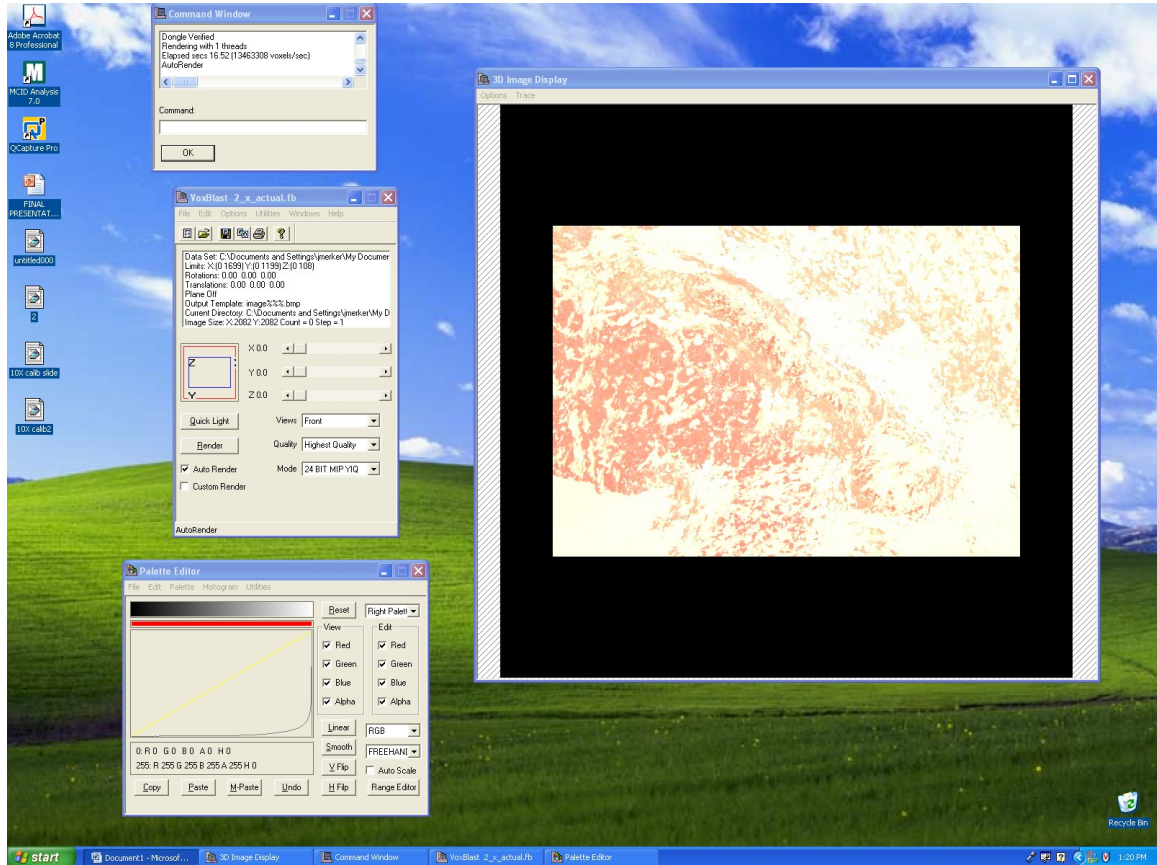
Figure 22. VoxBlast with a loaded data set.

Appendix B: Canceling Background in VoxBlast

What follows is a series of images showing how the background can be removed from the rendering, thereby allowing a better view of the desired subject. The goal of this exercise was to attempt to isolate the blood vessels found at the center of the slide. To accomplish this, a maximum intensity projection (MIP) algorithm is used, which basically allows the user to negate certain colors by minimizing its intensity. The bottom left window on the screen shots is called the color palette editor, and the yellow line passing through the middle of the graph is what controls the intensity of the colors by manipulating its shape. Figure 23 through 27 are basically a progression of removing the lighter background to expose the darker blood vessels.

Appendix B: (Continued)
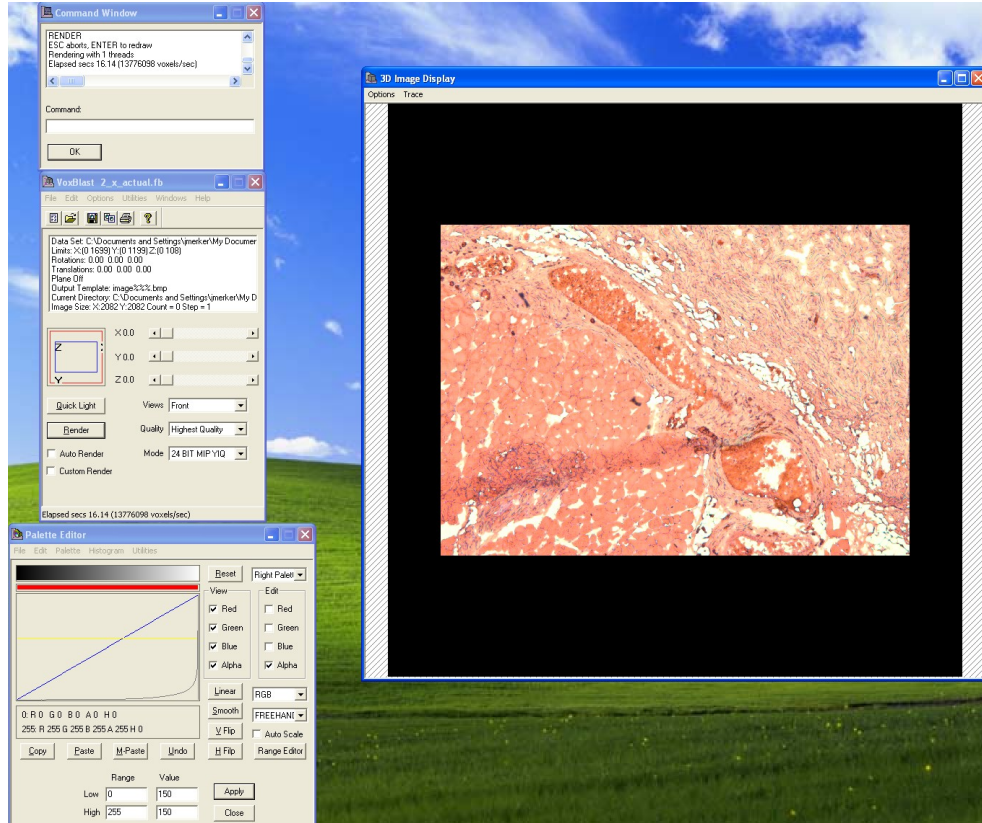
Figure 23. The palette editor in VoxBlast.
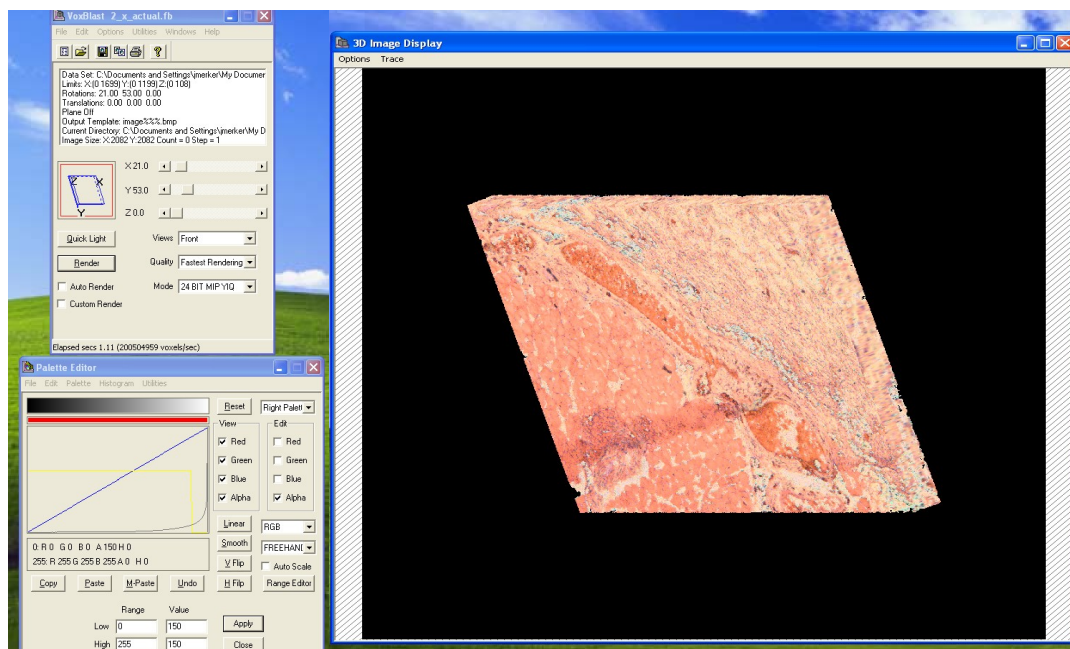
Appendix B: (Continued)

Figure 24. Turned volume with some background removed.
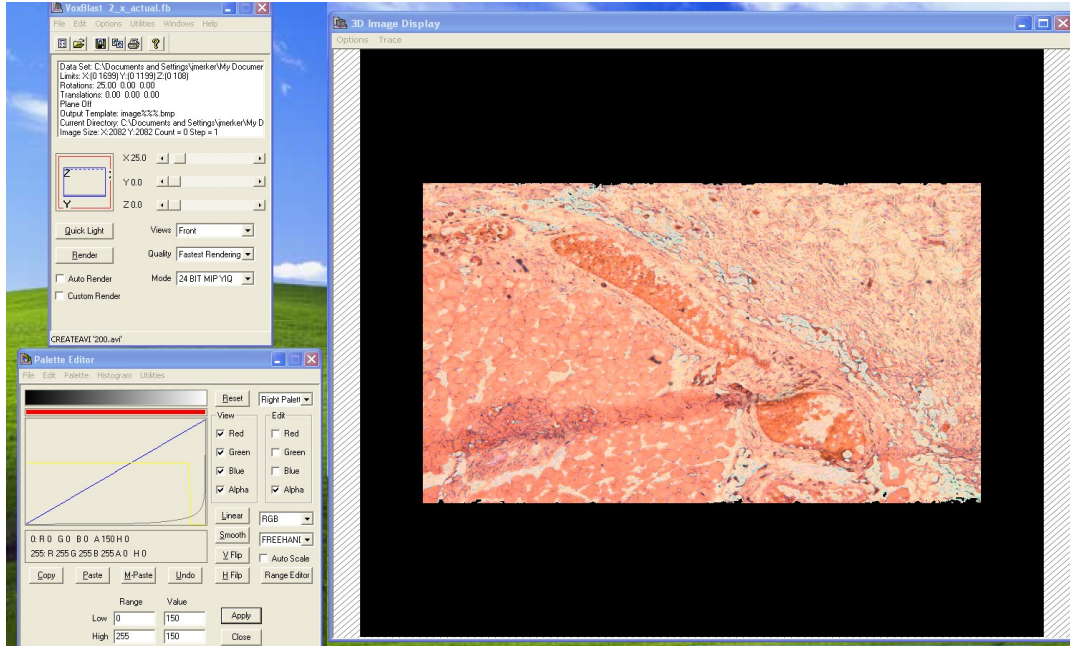
Appendix B: (Continued)

Figure 25. Another view of the solid with some background removed.
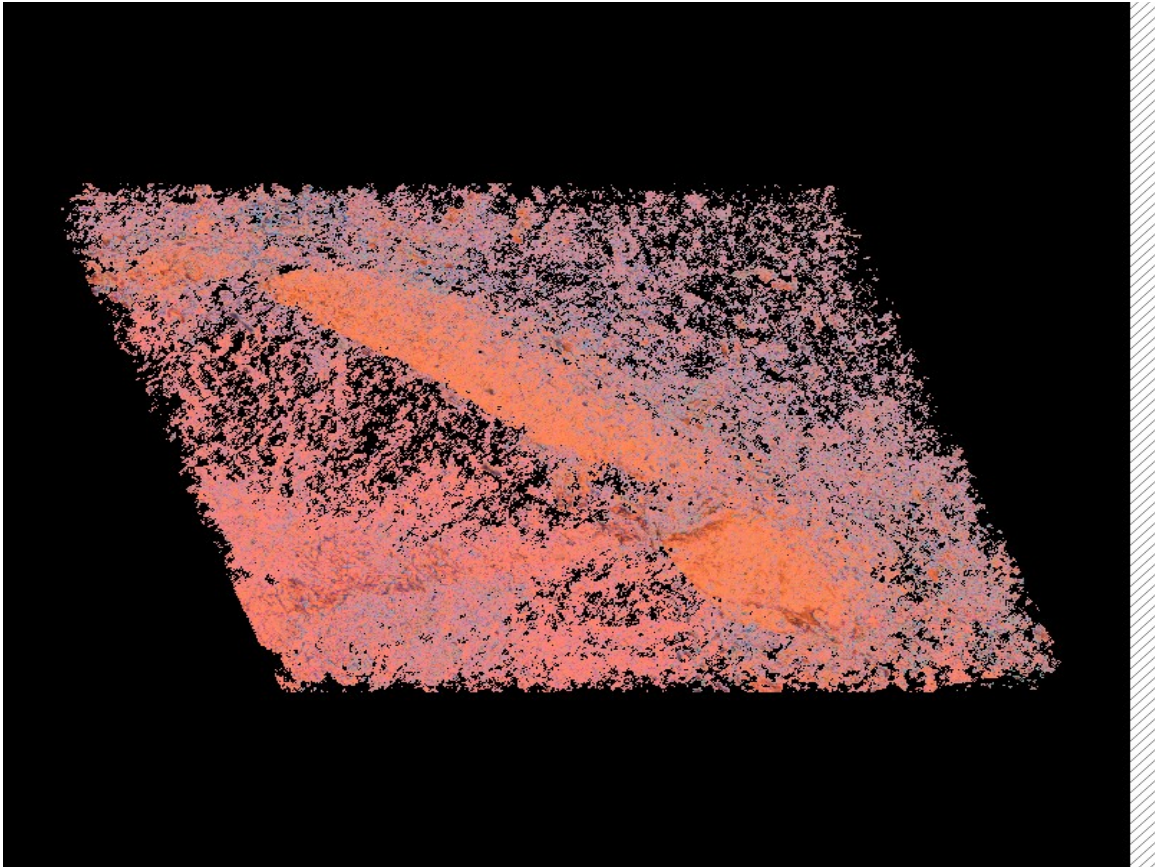
Appendix B: (Continued)

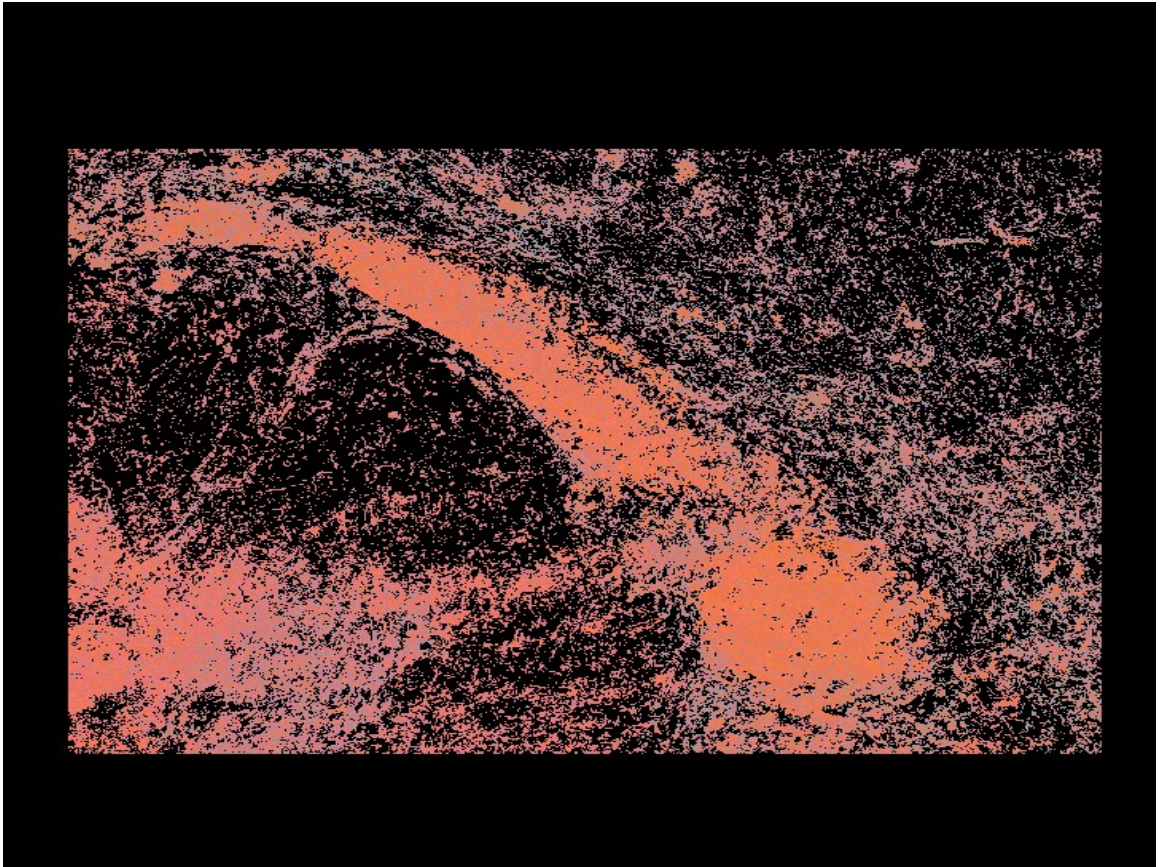Figure 26. View of the same solid with more background removed.

Figure 27. Same volume but with a majority of the background removed.

Appendix B: (Continued)

In the screen below, there is a new window at the lower center. This is the movie generation window, which allows for simple movies to be automatically saved in a number of formats. The generator is capable of capturing rotation about the X, Y, and/or Z axis.
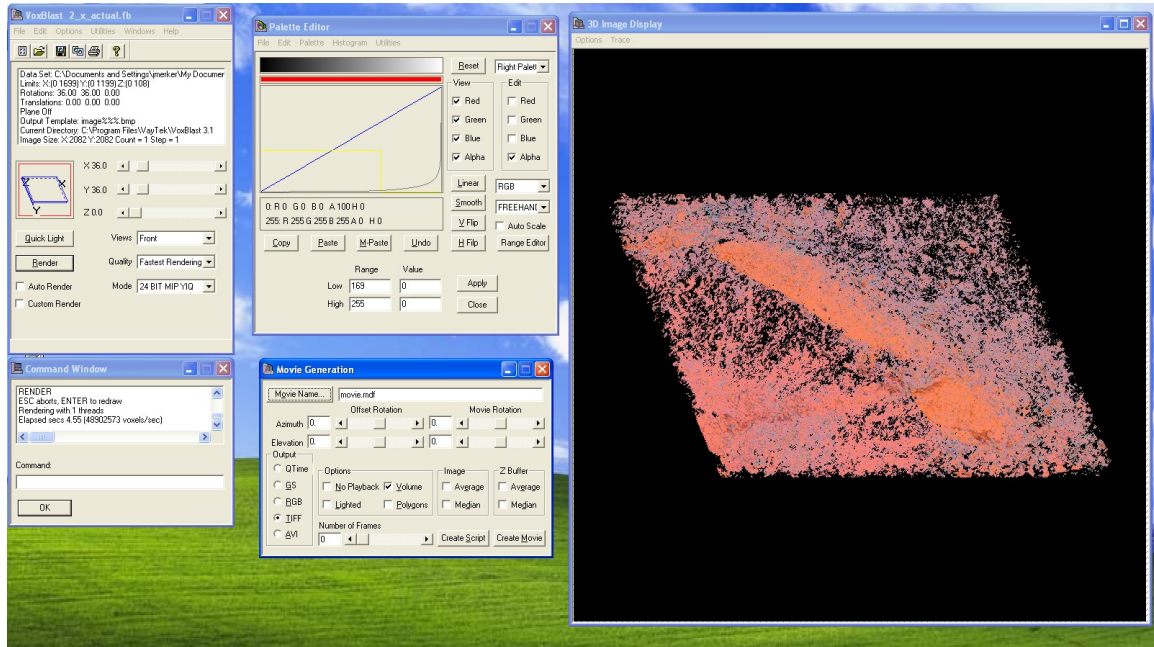

Figure 28. Movie generation window in VoxBlast.

Appendix B: (Continued)

Below is an example of another way to see through a sample. Instead of removing the background colors all together, a reverse ramp function is used to make the lighter colors much more transparent than the darker colors.
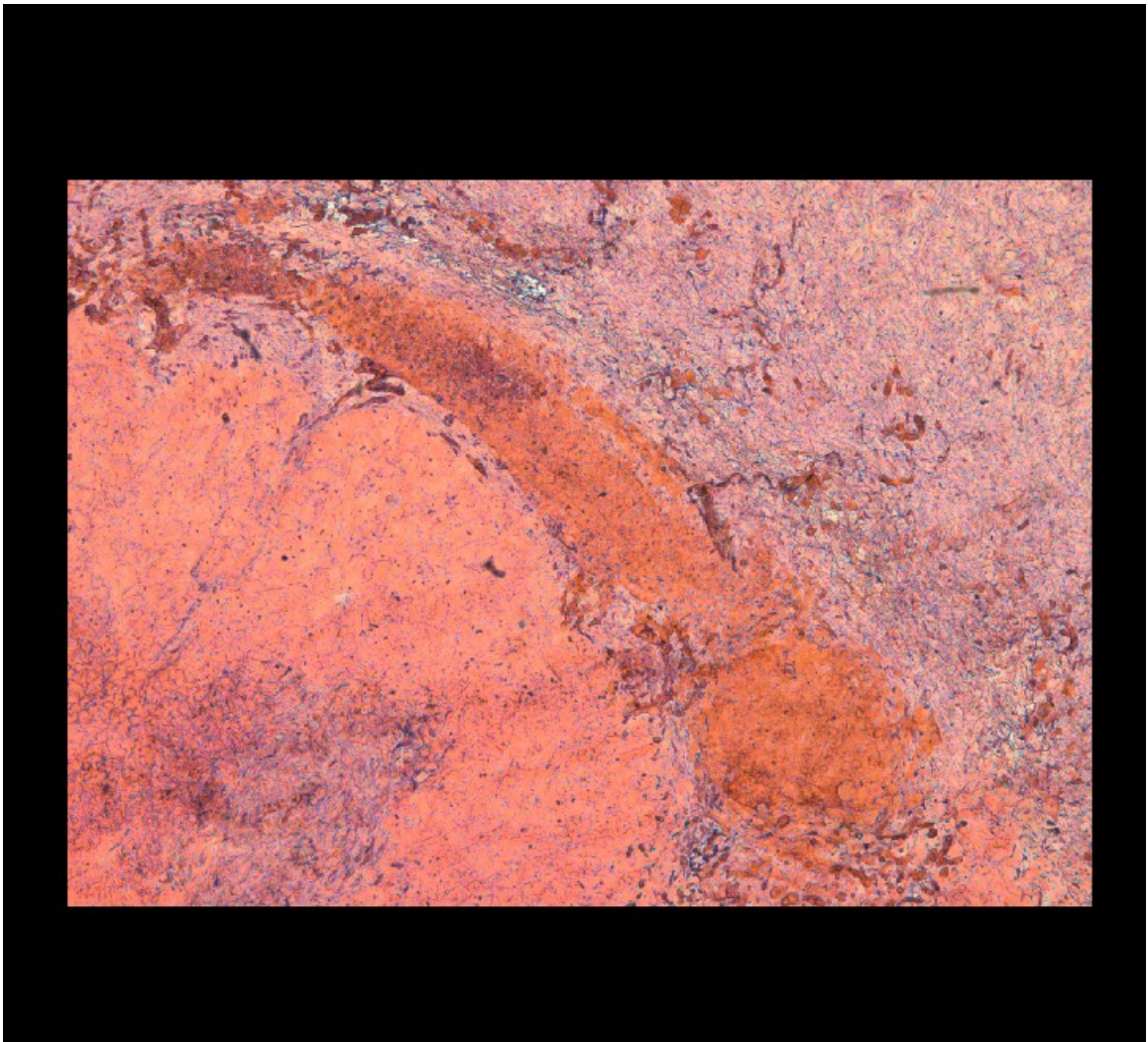

Figure 29. The color palette with a reverse ramp function.